

Strain rate sensitive microstructural evolution in a TRIP assisted high entropy alloy: Experiments, microstructure and modeling

Ravi Sankar Haridas^{a,b,c}, Priyanshi Agrawal^{a,b,c}, Saket Thapliyal^{a,b,c}, Surekha Yadav^{a,b,c} and Rajiv S. Mishra^{a,b,c,*}, Brandon A. McWilliams^d, Kyu C. Cho^d

^a Department of Materials Science and Engineering, University of North Texas, Denton, TX, 76207, USA

^b Center for Friction Stir Processing, University of North Texas, Denton, TX, 76207, USA

^c Advanced Materials and Manufacturing Processes Institute, , University of North Texas, Denton, TX, 76207, USA

^d Weapons and Materials Research Directorate, CCDC Army Research Laboratory, Aberdeen Proving Grounds, Aberdeen, MD, 21005, USA

*Corresponding author e-mail: Rajiv.Mishra@unt.edu

Abstract

Compressive response of a novel $\text{Fe}_{38.5}\text{Mn}_{20}\text{Co}_{20}\text{Cr}_{15}\text{Si}_5\text{Cu}_{1.5}$ high entropy alloy with transformation induced plasticity made by laser powder bed fusion was studied at quasi-static, medium and high strain rates. Mechanical response and variation in work hardening rate with strain rate were correlated with γ (f.c.c.) \rightarrow ϵ (h.c.p.) martensitic transformation, subsequent phase evolution and adiabatic heating. A strong near basal $\{0\ 0\ 0\ 1\}$ texture observed in the transformed ϵ (h.c.p.) phase after deformation was correlated with the initial texture, γ (f.c.c.) \rightarrow ϵ (h.c.p.) transformation orientation relationship as well as the activated deformation mechanisms in ϵ (h.c.p.) phase. The initial c/a ratio of 1.612 for the ϵ (h.c.p.) phase evolved with deformation and this was quantified to understand the propensity of non-basal $\langle c+a \rangle$ slip activation. Metastable γ (f.c.c.) dominant microstructure in the as-built alloy enabled excellent hardening via γ (f.c.c.) \rightarrow ϵ (h.c.p.) transformation accompanied by activation of non-basal $\langle c+a \rangle$ slip and twinning. Experimental results were correlated with existing empirical constitutive models such as Johnson-Cook, Modified Zerilli-Armstrong, Khan-Huang-Liang and Khan-Liu; the Khan-Liu model evidenced the best correlation with experimental results.

Keywords: *High entropy alloys; Transformation induced plasticity; Additive Manufacturing; High strain rate loading; Microstructures*

1 Introduction

The first two decades of the 21st century have witnessed remarkable advances in manufacturing and material science. Additive manufacturing (AM) has redefined the space occupied by conventional manufacturing techniques by virtue of its capability to fabricate intricate structural components on a large scale in different material categories (e.g. metals, ceramics, polymers and composites) with minimal material loss, design flexibility, minimum lead time and lesser end-product cost (Ngo et al., 2018). However, structural application of additively manufactured (AMed) components demands excellent strength-ductility synergy, fatigue resistance, fracture toughness and sometimes creep, wear and corrosion resistance. Nonetheless, AMed components are susceptible to structural deficiencies such as porosity, lack of fusion (LoF), micro-cracks and mechanical inhomogeneity in the form of structural anisotropy and residual stress (DebRoy et al., 2018). Such microstructural defects and inhomogeneity have resulted in deteriorated mechanical performance of AMed components for heavy-duty applications, thereby limiting comprehensive acceptance of AM. Extensive research enabled parametric optimization in AM materials and succeeded in limiting overall porosity within 1% (Hrabe et al., 2017; Kasperovich and Hausmann, 2015; Leuders et al., 2013; Siddique et al., 2017; Thapliyal et al., 2019). However, absolute exclusion of porosity during AM is still unfeasible even with the most recent advancements in AM. Hence, development of a defect-tolerant material for AM is crucial for its successful application.

Likewise, materials science also procured an enormous leap with the introduction of high entropy alloys (HEAs), otherwise called multi-component alloys or multi-principal element alloys (MPEAs) (Miracle and Senkov, 2017). Recent years have seen the expansion of HEAs into non-equiautomic compositional space, termed as complex concentrated alloys (CCAs). Flexibility in element selection and proportional elemental mixing in HEAs/CCAs enabled excellent strength-ductility synergy (Ding et al., 2019; Li et al., 2016; Zezhou Li et al., 2019), exceptional damage tolerance and fracture toughness (Gludovatz et al., 2016, 2014), high temperature properties (Senkov et al., 2010), outstanding wear resistance (Chuang et al., 2011; Yadav et al., 2018) and corrosion resistance (Qiu et al., 2013; Shi et al., 2017). Functionality of HEAs in structural applications by virtue of exceptional synergy of mechanical properties attracted the AM research community to investigate their efficacy in three-dimensional (3D)

printing. Printability, microstructural evolution, phase stability, texture, mechanical properties and corrosion properties of various HEAs comprising FeCoCrNi (Brif et al., 2015; Karthik et al., 2017; Zhou et al., 2018), FeCoCrNiMn (Guo et al., 2018; Haase et al., 2017; Li et al., 2018; Liu et al., 2013; Zhu et al., 2018) and $\text{Al}_x\text{CoCrFeNi}$ (Fujieda et al., 2015; Joseph et al., 2017; Kuwabara et al., 2018; Li et al., 2017) systems have been investigated widely.

Introduction of twinning induced plasticity (TWIP) and transformation induced plasticity (TRIP) have taken HEAs/HEAs to a new paradigm of strength and ductility. Recently, Li et al. (Li et al., 2016) introduced TRIP in a metastable dual phase (DP) HEA ($\text{Fe}_{80-x}\text{CoCrMn}_x$) and reported excellent strength-ductility synergy by coupling the solid solution hardening of HEAs and phase metastability-driven hardening. Inspired by the state of the art, Nene et al. (Nene et al., 2019; S. S. Nene et al., 2018; S.S. Nene et al., 2018a, 2018b) designed novel TRIP HEAs by tailoring the phase stability of f.c.c. γ -phase and subsequently the SFE by altering the Gibbs free energy change ($G^{\gamma \rightarrow \epsilon}$) for γ (f.c.c.) \rightarrow ϵ (h.c.p.) martensitic transformation by adding alloying elements such as Si, Cu and Al and obtained remarkable strength-ductility combinations. Further, Liu et al. (Liu et al., 2019, 2018) investigated the performance of such metastable alloys and reported exceptional performance under cyclic loading. Stress concentration (SC) ahead of fatigue crack tip enabled TRIP in its vicinity and subsequently resulted in sustained work hardening, thereby retarding the crack growth rate. In line with this, the crack retention ability in AMed TRIP DP-HEAs in the vicinity of micro voids and micro cracks through TRIP-driven sustained work hardening makes them an excellent candidate for damage-tolerant material for AM.

Outstanding mechanical performance of TRIP HEAs favoring structural applications motivated us to investigate the printability of such HEAs using laser powder bed fusion (LPBF) and further to investigate the mechanical response. Recently, Agrawal et al. (Agrawal et al., 2020) successfully printed a metastable $\text{Fe}_{40}\text{Mn}_{20}\text{Co}_{20}\text{Cr}_{15}\text{Si}_5$ (hereby denoted as CS-HEA) by LPBF with ϵ (h.c.p.) dominant microstructure and obtained exceptional strength of 1.15 GPa and ductility of 30% while keeping the porosity volume fraction contained to <0.1%. Further, Thapliyal et al. (Thapliyal et al., 2020) extended the applicability of LPBF to print TRIP-assisted $\text{Fe}_{38.5}\text{Mn}_{20}\text{Co}_{20}\text{Cr}_{15}\text{Si}_5\text{Cu}_{1.5}$ HEA (hereby denoted Cu-HEA). Contrary to AMed CS-HEA, AM of Cu-HEA resulted in a γ (f.c.c.) dominant microstructure as a result of rapid solidification at very high cooling rates (Thapliyal et al., 2020). Hence, a pronounced TRIP effect was achieved

due to which a tensile strength of 1.2 GPa was accomplished.

Components meant for structural applications are subjected mostly to dynamic or cyclic loads when in operation rather than monotonic loads. Hence, understanding the mechanical response of those materials is critical for such applications (Bhattacharyya et al., 2017; Zan Li et al., 2019; Madivala et al., 2019; Pandey et al., 2015; Pandya et al., 2020; Yin et al., 2020; Zhao et al., 2018). Although the research on HEAs has been rigorous among the material science community in the current decade, the investigation of high strain rate response of HEAs has been limited. Some of the alloy systems that have been investigated under high strain rate include AlCrCuFeNi₂ (Ma et al., 2016), NiCoCrFe (Gao et al., 2020; T. W. Zhang et al., 2020), CoCrFeNi (Huo et al., 2017), CrMnFeCoNi (Park et al., 2018; Yang et al., 2020), CoCuFeMnNi (Sonkusare et al., 2020), CoCrFeNiNb_x (Maity et al., 2018) Al_{0.3}CoCrFeNi (Gangireddy et al., 2018a) and Al_{0.1}CoCrFeNi (Gangireddy et al., 2018b). Although Basu et al. (Basu et al., 2018) studied the strain rate sensitivity on a Fe₅₀Mn₃₀Co₁₀Cr₁₀ TRIP-HEA, the strain rate sensitivity was negligible in the quasi-static regime (10^{-4} s⁻¹ - 5×10^{-3} s⁻¹) of consideration. However, a detailed investigation on the mechanical and microstructural response in TRIP-HEAs at high strain rate is still lacking. The present study investigated the uniaxial compression properties and microstructural evolution in AMed TRIP Cu-HEA for a range of strain rates from quasi-static (10^{-3} s⁻¹) to dynamic conditions (2.5×10^3 s⁻¹). Special emphasis was given to evolution of microstructural texture during deformation, progression of *c/a* ratio in the transformed ϵ (h.c.p) martensitic phase and the propensity of various deformation mechanisms in ϵ (h.c.p) phase.

2 Experimental methods

2.1 AM of Cu-HEA

AM of Cu-HEA was achieved through LPBF. Cu-HEA powder was procured from the Oerlikon AM where the pre-alloyed Cu-HEA pellets were gas atomized. Size of the atomized powder particles was between 15-45 μm . Alloy composition of the powder is provided in Table 1. Aconity 3D MIDI unit furnished with a fiber laser was used for LPBF of Cu-HEA powder. A rectangular block was printed at parameters summarized in Table 2; more details regarding AM of Cu-HEA are provided in (Thapliyal et al., 2020). Cubic compression specimens having dimensions $3.25 \times 3.25 \times 3.25$ mm³ were precisely machined out from the rectangular block using KENT WSi 200 wire electrical discharge machine.

Table 1: Alloy composition of as received Cu-HEA powder

Elements At. %	Fe	Mn	Co	Cr	Si	Cu
Nominal (%)	38.5	20	20	15	5	1.5
Actual (%)	40.2±1.1	18.6±1.2	19.5±1.3	15.0±1.2	5.3±1.5	1.5±1.0

Table 2: Optimized LPBF parameters for Cu-HEA

Laser power (W)	Scanning speed (mm/s)	Hatch distance (mm)	Layer thickness (mm)	Spot size (mm)	Angle of stripe rotation (degrees)
140	800	0.12	0.04	0.08	67

2.2 Mechanical characterization

Uniaxial compression tests on the cubic AMed Cu-HEA specimens were performed at strain rates 10^{-3} s $^{-1}$, 10^{-2} s $^{-1}$, 10^{-1} s $^{-1}$, 10^0 s $^{-1}$, 10^3 s $^{-1}$, 1.75×10^3 s $^{-1}$ and 2.5×10^3 s $^{-1}$. All specimens were compressed along the build direction.

2.2.1 Quasi-static and medium strain rate testing

Compression tests from quasi-static (10^{-3} s $^{-1}$) to medium strain rates (10^0 s $^{-1}$) were conducted on an MTS 322 load frame equipped with a 500 kN load cell. Experiments at strain rates of 10^{-3} s $^{-1}$ and 10^{-2} s $^{-1}$ were recorded at a sampling rate of 10 Hz using the MTS data acquisition system whereas those tested at 10^{-1} s $^{-1}$ and 10^0 s $^{-1}$ were recorded at a sampling rate of 0.5 kHz. An initial pre-load of 1 kN was applied consistently to all tested specimens to eliminate any slacking of compression jaws. Several specimens were tested to different axial strains at a specific strain rate to study the evolution of microstructure as a function of strain rate and axial strain. Additionally, to ensure repeatability of test data, three tests were performed at each strain rate for those specimens deformed up to failure. And, to avoid any interaction based inhomogeneity during the tests, proper care was taken to lubricate specimen surfaces in contact with compression jaws.

2.2.2 High strain rate testing

High strain rate compression tests were performed on a split-Hopkinson pressure bar (SHPB) procured from REL Inc. SureTest Systems. The SHPB experimental set-up (Fig. 1(a)) consists of

a striker bar, an incident bar and a transmitter bar made of high-strength maraging steel rods. The test specimen was sandwiched between the incident and transmitter bars. Resistance strain gauges were installed midway along the length on both incident and transmitter bars to record strain pulses. Strain signals measured by strain gauges connected to a Wheatstone bridge circuit were amplified using a Vishay 2300 signal conditioning amplifier system and were recorded further using a PicoScope® oscilloscope at a sampling rate of 1 MHz. The striker bar fired at specified velocity from an air gun equipped with compressed air supply, and coaxially struck the incident bar. The impact generated a compressive strain pulse ($\varepsilon_i(t)$) in the incident bar that propagated towards the incident bar-specimen interface at the elastic wave velocity of the bar (C_b). A portion of the incident compressive strain pulse deformed the specimen and moved into the transmitter bar as a transmitted compressive pulse ($\varepsilon_t(t)$). The remaining portion of the incident pulse was reflected from the incident bar-specimen interface as a reflected tensile pulse ($\varepsilon_r(t)$) and propagated towards the free end of the incident bar. A momentum trap assembly was also installed to eliminate multiple loading of the specimen. The nature of the recorded pulses is indicated in Fig. 1(b). The specimen strain ($\varepsilon_s(t)$) and stress ($\sigma_s(t)$) were obtained from the recorded strain pulses using Eq. 1 and Eq. 2 (Chen et al., 1999; Ravi Sankar and Parameswaran, 2016), respectively.

$$\varepsilon_s(t) = \frac{-2C_b}{L_s} \int_0^t \varepsilon_r(t) dt. \quad (1)$$

$$\sigma_s(t) = \frac{E_b A_b}{A_s} \int_0^t \varepsilon_t(t) dt. \quad (2)$$

$$C_b = \sqrt{\frac{E_b}{\rho_b}}. \quad (3)$$

where E_b and ρ_b are elastic modulus and the density of the bar material, respectively; L_s and A_s are specimen length and cross-sectional area, respectively; and A_b is the area of cross section of the bar. Furthermore, dynamic equilibrium (Eq. 4) during the experiment was monitored

$$\varepsilon_i + \varepsilon_r = \varepsilon_t. \quad (4)$$

consistently to ensure the validity of compression tests (Fig. 1(c)) (Gama et al., 2004).

Three different strikers, viz. 0.15 m, 0.3 m and 0.6 m, were used to vary loading pulse duration during the tests and thus controlled the final deformation of the specimen. The SHPB equipped with an infrared-photodiode sensor enabled precise velocity measurement for each striker so that

the same strain rate was achieved in all three cases. Each of the striker was fired at 6.5 m/s, 11 m/s and 17.5 m/s to achieve strain rates of 10^3 s $^{-1}$, 1.75×10^3 s $^{-1}$ and 2.5×10^3 s $^{-1}$, respectively. To ensure reproducibility of results, as with MTS tests, three tests were performed at all strain rates.

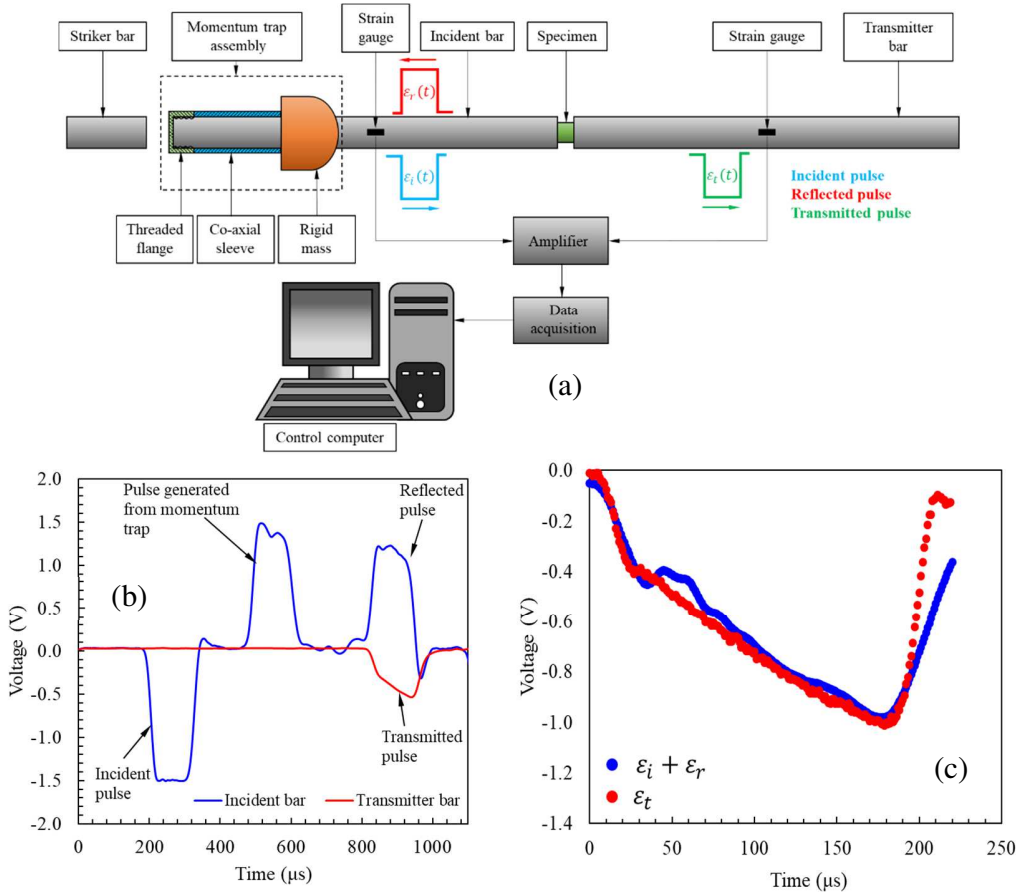


Figure 1: (a) Schematic diagram of SHPB experimental setup, (b) a typical SHPB strain gauge record, and (c) representative image illustrating dynamic equilibrium achieved during the SHPB experiment (voltage equivalent).

2.2.3 Microstructural characterization

Microstructural characterization using electron backscatter diffraction (EBSD) of both as-built and deformed specimens was performed in a FEI Nova Nano SEM 230 equipped with a Hikari Super EBSD detector functioning at an operating voltage of 20 kV. TEAM® software was used for data acquisition of EBSD data and the post analysis of the data was carried out in OIM TSL 8 software. Typical scan area and step size for the EBSD scans were $150 \times 120 \mu\text{m}^2$ and $0.5 \mu\text{m}$, respectively. Scanning parameters were kept constant for EBSD scans performed of all specimens. Phase fractions reported from EBSD analysis were averaged from three scans performed at different locations on the specimen.

X-ray diffraction (XRD) measurements of both as-built and deformed specimens were accomplished using a Rigaku Ultima III diffractometer and Cu K- α beam functioning at 40 kV and 44 mA. The peak positions (2θ) of both ϵ (h.c.p.) and γ (f.c.c.) phases were noted, and interplanar spacing d_{hkl} was computed using Bragg's law as follows.

$$d_{hkl} = \frac{\lambda}{2 \sin \theta}. \quad (5)$$

where, λ is the X-ray wavelength. Further, lattice parameters for the γ (f.c.c.) and ϵ (h.c.p.) phases were obtained using Eq. 6 and Eq. 7, respectively.

$$\frac{1}{(d_{hkl})_{f.c.c.}} = \frac{\sqrt{h^2+k^2+l^2}}{a_{f.c.c.}}. \quad (6)$$

$$\frac{1}{(d_{hkl})_{h.c.p.}^2} = \frac{4}{3} \left(\frac{h^2+hk+k^2}{(a_{h.c.p.})^2} \right) + \frac{l^2}{(c_{h.c.p.})^2}. \quad (7)$$

$a_{f.c.c.}$, $a_{h.c.p.}$ and $c_{h.c.p.}$ are respectively the lattice parameters of f.c.c. and h.c.p. crystal structures. $a_{f.c.c.}$ was computed from the respective (1 1 1) and (2 0 0) f.c.c. peaks in XRD data whereas $a_{h.c.p.}$ and $c_{h.c.p.}$ were calculated from the respective (1 0 0) and (1 0 1) h.c.p. peaks in the XRD data. Afterwards, c/a ratio for the h.c.p. phase was determined from $a_{h.c.p.}$ and $c_{h.c.p.}$ values.

X-ray microscopy (XRM) using a Zeiss Xradia Versa 520 X-ray microscope was performed on a cubic compression specimen. The purpose of performing XRM was to understand the evolution of internal pores and micro-cracks upon compression. To attain this, two XRM scans were performed: one on undeformed as-built specimen and another on the same specimen deformed to 30% strain level at 10^{-3} s $^{-1}$. A full field of view scan was achieved to acquire 2400 projections at 4X objective. The voxel size was set to 3.2 μm , voltage was set to 160kV and current was set to 62mA for both the scans. The exposure time for scanning undeformed specimen was set to 1.5 s while that for scanning deformed specimen was 1.0 s. Post analysis of XRM data was achieved using Dragonfly software.

3 Results and discussion

3.1 Microstructure of as-built Cu-HEA

Thapliyal et al. (Thapliyal et al., 2020) studied solidification characteristics of Cu-HEA and reported a high hot susceptibility index (HSI) and freezing range (FR) that resulted hot cracks in the microstructure after AM. However, the crack and pore volume fraction was restricted to

1.5%. Figure 2 (a), a schematic diagram of the printed block, indicates the direction of build (z). Figures 2 (b) and 2 (c) represent the EBSD micrographs indicating inverse pole figure (IPF) of the as-built microstructure in the build and transverse ($x-y$ plane) directions, respectively. The large fraction of columnar grains evident along the build direction is attributed to its high HSI and FR (Thapliyal et al., 2020). The morphological variation of grains in the transverse direction (Fig. 2 (c)) clearly indicated a microstructural anisotropy in the as-built Cu-HEA. The EBSD map depicts the initial γ (f.c.c.) - ϵ (h.c.p.) phase fraction in the alloy (Fig. 2 (d)). A γ (f.c.c.) dominant microstructure was obtained after AM with 94% γ (f.c.c.) and 6% ϵ (h.c.p.) phases. The rapid solidification and cooling rate during AM may have prompted uniform dissolution of Cu in the solid solution, and thus stabilized the γ (f.c.c.) phase upon cooling (Thapliyal et al., 2020). The higher γ (f.c.c.) fraction in printed Cu-HEA is expected to assist a pronounced TRIP effect upon deformation (Nene et al., 2019). Figure 2(e), the XRD data of the as-built alloy, presents the corresponding γ (f.c.c.) and ϵ (h.c.p.) peaks.

Figure 3 (a) shows the EBSD micrograph of the as-built microstructure indicating the IPF along the axis of build. The IPF map of γ (f.c.c.) phase grains along the axis of build (Fig. 3(b)) indicates a dominant dual texture towards {1 1 1} and {1 0 1} crystallographic orientations. In f.c.c. crystals, during rapid solidification of the melt pool on a polycrystalline substrate, the epitaxial growth of columnar grains is preferred along one of the six $<0\ 0\ 1>$ crystallographic directions governed by the maximum local heat flow direction (Kurz and Fisher, 1998; Rappaz and Blank, 1986; Wei et al., 2015). Further, the solidification direction of grains with respect to the build direction also depends on the laser scanning strategy used during AM (Wei et al., 2015). Unidirectional scanning strategy in successive layers oriented the columnar dendrites at 60° to the build direction, whereas bidirectional scanning strategy resulted in $\pm 45^\circ$ orientation between successive layers (Wei et al., 2015). Columnar grains in the as-printed Cu-HEA after solidification were oriented mostly at 25° - 65° to the axis of build rather than a specific orientation, owing to the striped scan strategy with 67° rotation angle between successive layers used during LPBF (Fig. 3 (c)). A schematic representation of a crystal oriented at 45° to the build direction (Fig. 3 (d)) points to grain growth along the [0 0 1] direction. Such a directional grain growth aligns the normal of $(1\ 0\ \bar{1})$ plane (plane DBFH) parallel to the build direction, the angle between both planes being 45° . This relationship holds for all grains oriented at 45° to the build direction in 3D (assuming a 3D melt pool), resulting in a {1 0 1} texture of such grains on the

transverse section. Likewise, {1 1 1} set of equivalent planes aligns parallel to the transverse

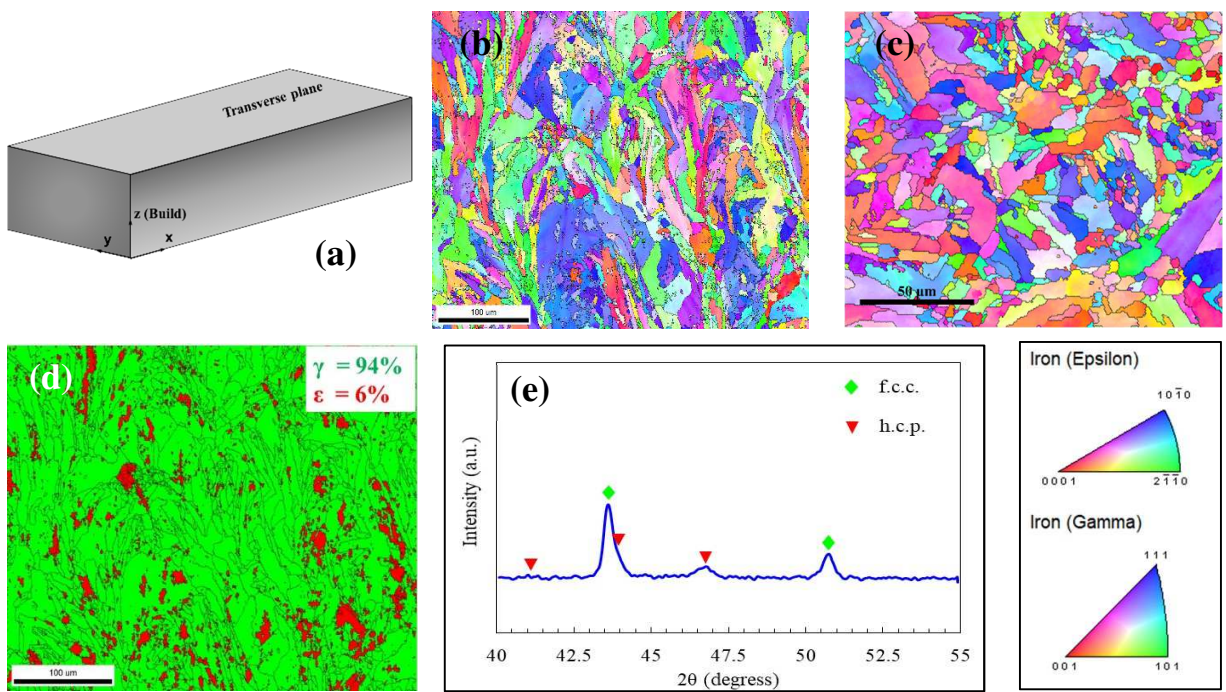


Figure 2: (a) schematic of printed Cu-HEA block indicating the build direction, (b) IPF map showing the microstructure in the build direction of as-built material, (c) IPF map showing the microstructure in transverse direction of the as-built material, (d) EBSD image showing the phase fraction in as-built material, and (e) XRD data of the as-built material indicating the corresponding γ and ϵ peaks.

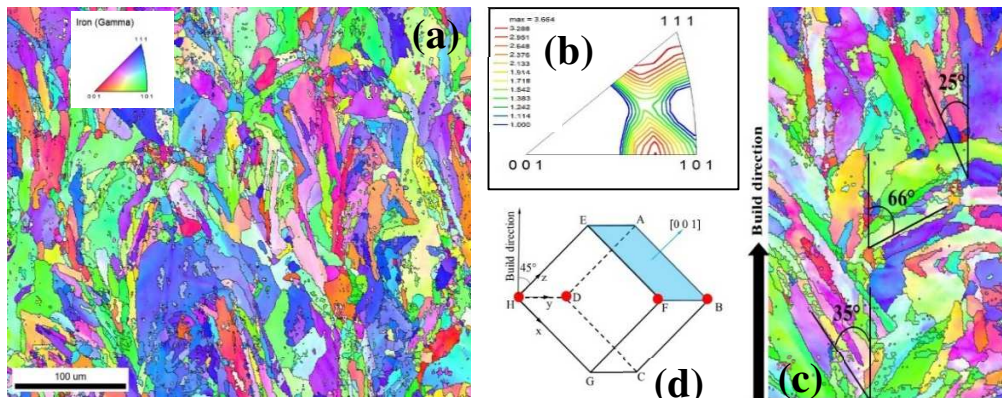


Figure 3: (a) EBSD map indicating the IPF along the axis of build, (b) texture along the axis of build in the as-built Cu-HEA indicated in the form of IPF map, (c) microstructure along the build direction indicating the orientation of columnar grains with the axis of build, and (d) schematic of a f.c.c. unit cell showing the growth direction with respect to build direction and the plane DBFH with its normal along the axis of build.

section in grains oriented at $\sim 55^\circ$ to the build direction, and resulting in a $\{111\}$ texture of such

grains on the transverse section. Hence, the columnar grains being mostly oriented at 25°–65° to the build direction resulted in a dominant dual crystallographic texture along the axis of build with an intensity towards {1 1 1} and {1 0 1} crystallographic orientations (Fig. 3(b)).

3.2 Mechanical response

The engineering stress-strain response at different strain rates is given in Fig. 4 (a). The material yielded at 510 MPa at 10^{-3} s $^{-1}$ and exhibited substantial work hardening, reaching an ultimate strength of 2.75 GPa (engineering stress) at failure. Engineering stress-strain response of Cu-HEA at high strain rates tested in SHPB along with the corresponding strain rate variation during compression (data is for 0.3 m striker), indicate a positive strain rate sensitivity, i.e., an increase in flow stress with strain rate for a specific axial strain (Fig. 4 (b)). With particular emphasis, note that strain rate varies during compressive loading of the specimen in SHPB; and strain rate values reported are average value during the loading span. Strain rate sensitivity on compressive yield strength of the material was marginal from quasi-static (10^{-3} s $^{-1}$) to near dynamic (10^0 s $^{-1}$) strain rates (the strain rate sensitivity exponent, $[d(\ln \sigma)/d(\ln \dot{\epsilon})]_{\epsilon=\text{constant}}$, $m = 0.007$); whereas at higher strain rates (10^3 s $^{-1}$ – 2.5×10^3 s $^{-1}$) the strain rate sensitivity was significantly high with $m = 0.18$ (Fig. 4 (c)). True stress–true strain response and corresponding work hardening rate of the material at 10^{-3} s $^{-1}$ – 10^{-1} s $^{-1}$ revealed negligible strain rate sensitivity on flow stress for which the value of $m = 0.005$, 0.004 , 0.004 and 0.003 at 10% , 20% , 30% and 40% true strain levels, respectively (Fig. 4 (d)). Of special emphasis is that, the true stress–true strain response at 10^0 s $^{-1}$ (near dynamic) indicated negative strain rate sensitivity on flow stress when compared with quasi-static response (10^{-3} s $^{-1}$) of the material at strain levels $>20\%$ (Fig. 4 (d)). Peculiar crossover of stress-strain curves designating a negative rate sensitivity was also observed (black markers in inset of Fig. 4 (d)). The value of m varied from 0.0004 at 20% plastic strain to -0.024 at 60% plastic strain between flow stress-plastic strain curve corresponding to 10^{-3} s $^{-1}$ and 10^0 s $^{-1}$. Although compressive yield strength of the material was higher at high strain rates, work hardening ability of the material reduced, as is evident from the work hardening rate curves at 10^0 s $^{-1}$ and 2.5×10^3 s $^{-1}$ (Fig. 4 (d)).

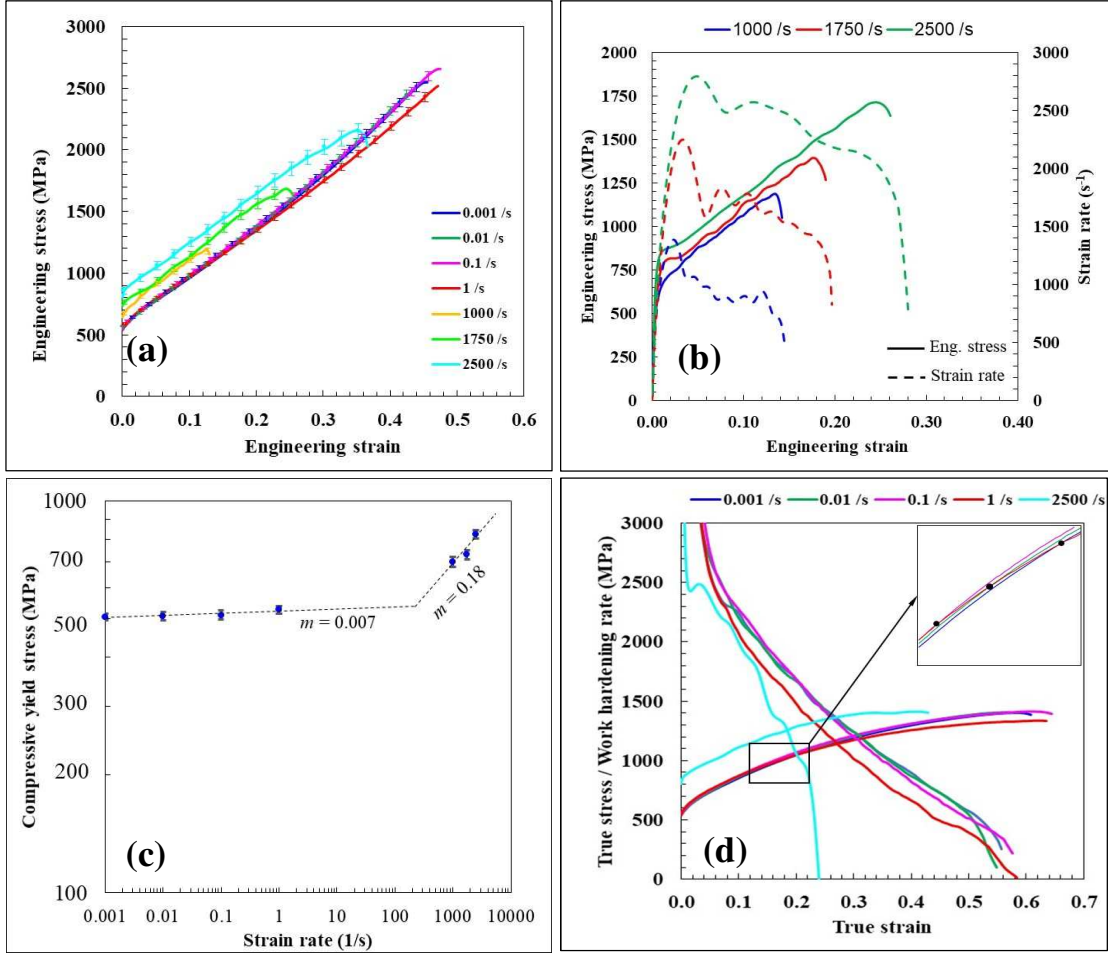


Figure 4: Compressive mechanical response of AMed Cu-HEA. (a) Engineering stress-strain response at strain rates from 10^{-3} s $^{-1}$ to 2.5×10^3 s $^{-1}$ (note the error bar using three tests to denote the significant increase in stress level at high strain rates), (b) engineering stress-strain response and corresponding strain rate variation at high strain rates, (c) compressive yield stress variation with strain rate, and (d) true stress-strain response and work hardening rate of AMed Cu HEA from 10^{-3} s $^{-1}$ – 10^0 s $^{-1}$ and 2.5×10^3 s $^{-1}$. (Inset of Fig. 4 (d) shows the crossover of true stress-true strain response at 10^0 s $^{-1}$ where black markers indicate locations of crossover).

3.3 Evolution of microstructure

Microstructural evolution of the AMed Cu-HEA was further analyzed to understand its influence on the variation of strain hardening with strain rate, specifically the influence of TRIP on hardening at different strain rates. Sinha et al. (Sinha et al., 2020) theoretically studied the contribution of different hardening modes in TRIP CS-HEA, modes such as dislocation based hardening, geometric hardening due to lattice re-orientation, hardening due to TRIP/twin; and major hardening contribution was due to strain induced γ (f.c.c.) $\rightarrow\epsilon$ (h.c.p.) transformation. Hence, microstructural evolution based on strain induced γ (f.c.c.) $\rightarrow\epsilon$ (h.c.p.) transformation as a

function of strain and strain rate was analyzed. Figures 5 (a1–a4), 5 (b1–b4) and 5 (c1–c3) show the evolution of transformation at 10^{-3} s⁻¹, 10^0 s⁻¹ and 2.5×10^3 s⁻¹, respectively. Figure 5 (d) summarizes the percentage reduction in γ (f.c.c.) as a function of strain at different strain rates. The resemblance of stress-strain response at 10^{-3} s⁻¹ and 10^1 s⁻¹ (Fig. 4 (d)) as reflected in the percentage reduction in γ (f.c.c.) phase, indicates that the hardening contribution due to TRIP at both strain rates is similar. However, a considerable reduction in percentage change in γ (f.c.c.) phase at 10^0 s⁻¹ and 2.5×10^3 s⁻¹ compared to 10^{-3} s⁻¹ indicated a lower contribution of TRIP towards hardening, due to which a lower work hardening rate occurred at those strain rates (Fig. 4 (d)). Under near-dynamic and dynamic conditions, adiabatic heating becomes important. The heat conduction inside the specimen is negligible due to the absence of a thermal gradient. Under such conditions, a substantial temperature rise inside the specimen resulted in thermal softening in HEAs (Soares et al., 2019). The temperature rise inside the material can be calculated using (Soares et al., 2019),

$$\Delta T(\varepsilon) = \frac{\beta \int_0^\varepsilon \sigma d\varepsilon}{\rho C_p}. \quad (8)$$

where ΔT is the temperature rise, β is the Taylor-Quinney co-efficient, C_p is the specific heat capacity of the material and ρ is the material density. Values of $\rho = 7.655$ g/cc (experimentally determined) and $C_p = 430$ J/(kg.K) (Wang et al., 2016) were used to calculate ΔT . Although in literature, the value of β was assumed mostly as 0.9, a recent comprehensive work on the evolution of β in FeCoCrMnNi HEA at high strain rates reported an average value of $\beta=0.6$ during deformation (Soares et al., 2019), which is used in the present study. Increase in temperature during high strain rate deformation is appreciable, in that it reaches a value $>100^\circ\text{C}$ at 50% true strain (Fig. 5 (e)). Additionally, rate of transformation at strains above 25% at 10^0 s⁻¹ and 2.5×10^3 s⁻¹ was sluggish as evident from the nearly flat nature of the curves corresponding to those strain rates (green and red curves in Fig. 5 (d)), owing to a significant increase in $\Delta T > 50^\circ\text{C}$ that causes thermal softening (Fig. 5 (e)). Hence, the conclusion is that sluggish γ (f.c.c.) \rightarrow ϵ (h.c.p.) transformation in addition to thermal softening due to prevailing adiabatic heating resulted in a reduction in hardening rate of AMed Cu-HEA at high strain rates.

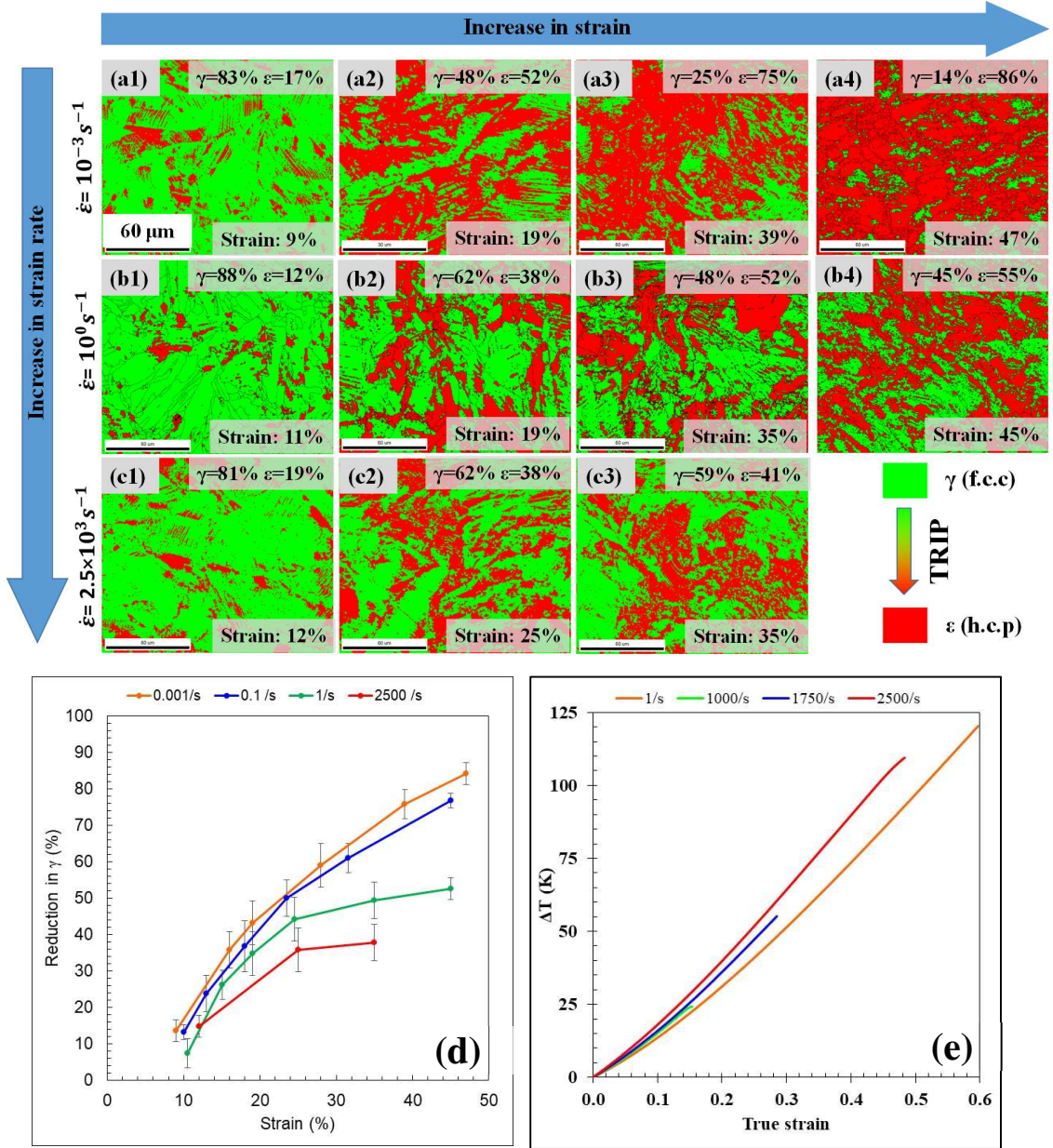


Figure 5: The ϵ phase evolution as a function of strain at 10^{-3} s^{-1} (a1-a4), 10^0 s^{-1} (b1-b4) and $2.5 \times 10^3 \text{ s}^{-1}$ (c1-c3), (d) percentage reduction in γ as a function of strain at different strain rates, and (e) temperature rise in the compression specimen due to adiabatic heating.

Further analysis increased understanding of the texture evolution in the transformed ϵ (h.c.p.) grains. γ (f.c.c.) \rightarrow ϵ (h.c.p.) transformation follows the Shoji-Nishiyama (S-N) orientation relationship (OR), and can be represented as follows (Nishiyama, 1978),

$$(1\ 1\ 1)_\gamma // (0\ 0\ 0\ 1)_\epsilon \text{ and } [1\ 0\ \bar{1}]_\gamma // [1\ 1\ \bar{2}\ 0]_\epsilon. \quad (9)$$

Under S-N OR, during γ (f.c.c.) \rightarrow ϵ (h.c.p.) transformation, $(1\ 1\ 1)$ plane of f.c.c. transforms to

the basal $(0\ 0\ 0\ 1)$ plane of h.c.p., and $[1\ 0\ \bar{1}]$ direction of f.c.c. aligns parallel to $[1\ 1\ \bar{2}\ 0]$ direction of h.c.p. through atomic rearrangement. Otherwise, the f.c.c. grains with $(1\ 1\ 1)$ texture along a specific direction, when transformed, will have a $(0\ 0\ 0\ 1)$ basal texture in the transformed h.c.p. grain along the same direction. S-N OR was reported in TRIP HEAs in a previous study as well (Sinha et al., 2019). Figures 6 (a–b) shows the S-N OR observed in AMed Cu-HEA used for the current study (grains enclosed by ellipses) supported by the $(1\ 1\ 1)_{\text{f.c.c.}}$ and $(0\ 0\ 0\ 1)_{\text{h.c.p.}}$ pole figures of the grains enclosed by the black ellipse (Figs. 6 (c–d)). A schematic of the planes that become parallel during the transformation (Fig. 6 (e)) specifies where plane $(\text{AFH})_{\text{f.c.c.}}/\!/(\text{MNOPQR})_{\text{h.c.p.}}$.

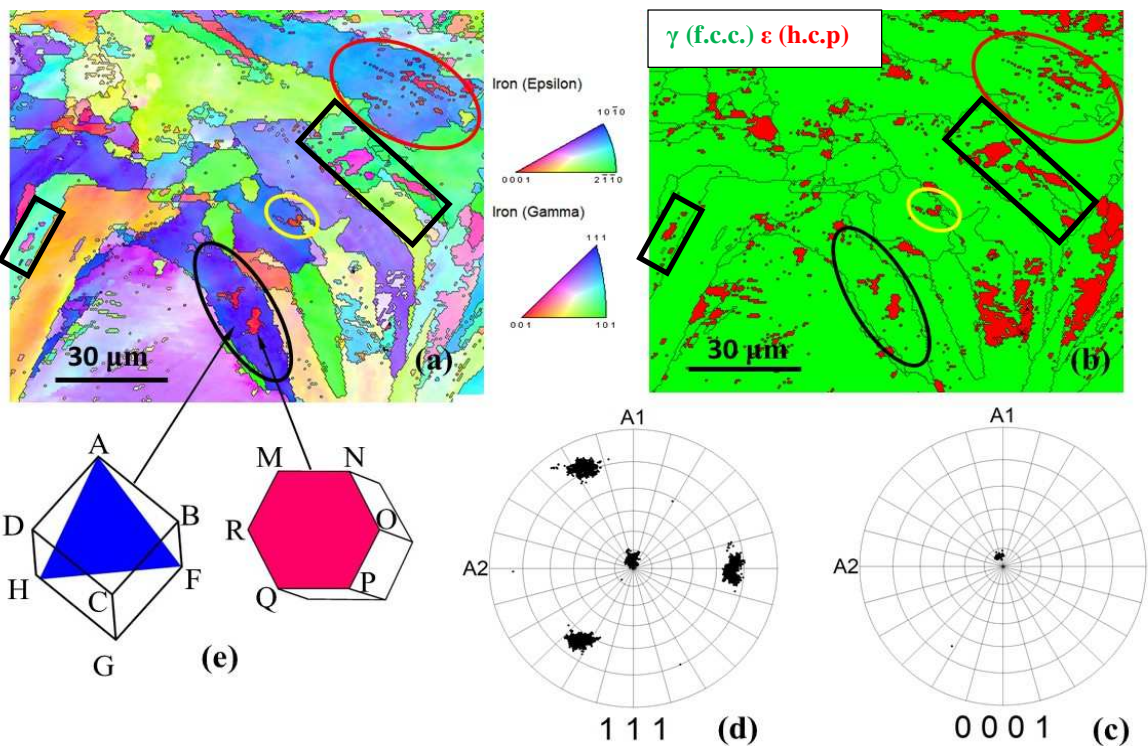


Figure 6: (a) IPF map showing the S-N OR in the grains enclosed by the ellipses, (b) corresponding phase map, (c) $(0\ 0\ 0\ 1)$ h.c.p. pole figure of the ϵ grains enclosed by the black ellipse (d) $(1\ 1\ 1)$ f.c.c. pole figure of the γ grain enclosed by the black ellipse, and (e) schematic diagram showing $(1\ 1\ 1)$ and $(0\ 0\ 0\ 1)$ plane orientations in f.c.c. and h.c.p. unit cell where plane $\text{AFH}_{\text{f.c.c.}}/\!/(\text{MNOPQR}_{\text{h.c.p.}})$.

Figures 7 (a1–a4) are EBSD micrographs showing the IPF that indicate the texture evolution in the transformed ϵ (h.c.p.) grains, with deformation at $10^{-3}\ \text{s}^{-1}$. Further, the evolved texture is also displayed in the form of IPF maps (Figs. 7 (b1–b4)). Clearly, a prominent texture concentrated towards the $(0\ 0\ 0\ 1)$ basal pole is evident. The pole figure map of the ϵ (h.c.p.) grains obtained

on a section transverse to the axis of compression also confirmed a strong near-basal texture (Fig. 7 (c)). As described in Fig. 3, the as-built microstructure indicated a dual texture towards {1 1 1} and {1 0 1} f.c.c. poles along the axis of build (loading axis). Under uniaxial compression of the material along the axis of build, the {1 1 1} textured γ (f.c.c.) phase grains transformed to ϵ (h.c.p.) phase, during which the S-N OR was complied, and thus resulted in a {0 0 0 1} h.c.p. basal texture along the axis of compression. Similarly, the {1 0 1} textured γ (f.c.c.) grains also underwent transformation and culminated in a near-basal texture in the ϵ (h.c.p.) phase (black rectangular boxes in Figs. 6 (a–b)). Hence, the transformation of γ (f.c.c.) phase with a predominant {1 1 1} and {1 0 1} dual texture in the AMed alloy along the axis of build, in accordance with S-N OR, resulted in a strong near-basal {0 0 0 1} texture in the transformed ϵ (h.c.p.) phase. Additionally, the near-basal texture became stronger with deformation (Figs. 7 (b1–b4)). The reason for this trend is explored in section 3.5. The strong near-basal texture in ϵ (h.c.p.) phase was observed in specimens deformed at all strain rates (corresponding EBSD micrographs are shown in supplementary data Fig. S1).

Figure 7 (d1) is an XRM image obtained from a section perpendicular to the build direction in the as-built alloy and Fig. 7 (d2) is the image at the same cross-section after deforming the specimen to 30% strain at 10^{-3} s⁻¹. Acquisition of XRM images at the same cross-section assists in understanding the evolution of internal defects upon deformation in AMed components. Since the voxel size is kept constant for acquiring both the images shown in Figs. 7 (d1) and 7 (d2), the hazy appearance of pores in Fig. 7 (d2) indicates the reduction in pore size upon compression. This is confirmed by the porosity vol.% analysis for as-built specimen in both undeformed and deformed condition. Figures 7 (d3) and 7 (d4) show the magnified reconstructed 3D distribution of porosity within the undeformed and deformed specimen, respectively. The vol.% of pores and microcracks in undeformed specimen is ~1.2% whereas that in deformed specimen is ~0.4%. The vol.% obtained here holds good only for pores and microcracks with dimensions of at least ~7 μm . Nevertheless, it is safe to say that upon compression, pore closure occurs due to plastic flow of material and the pore vol.% decreases.

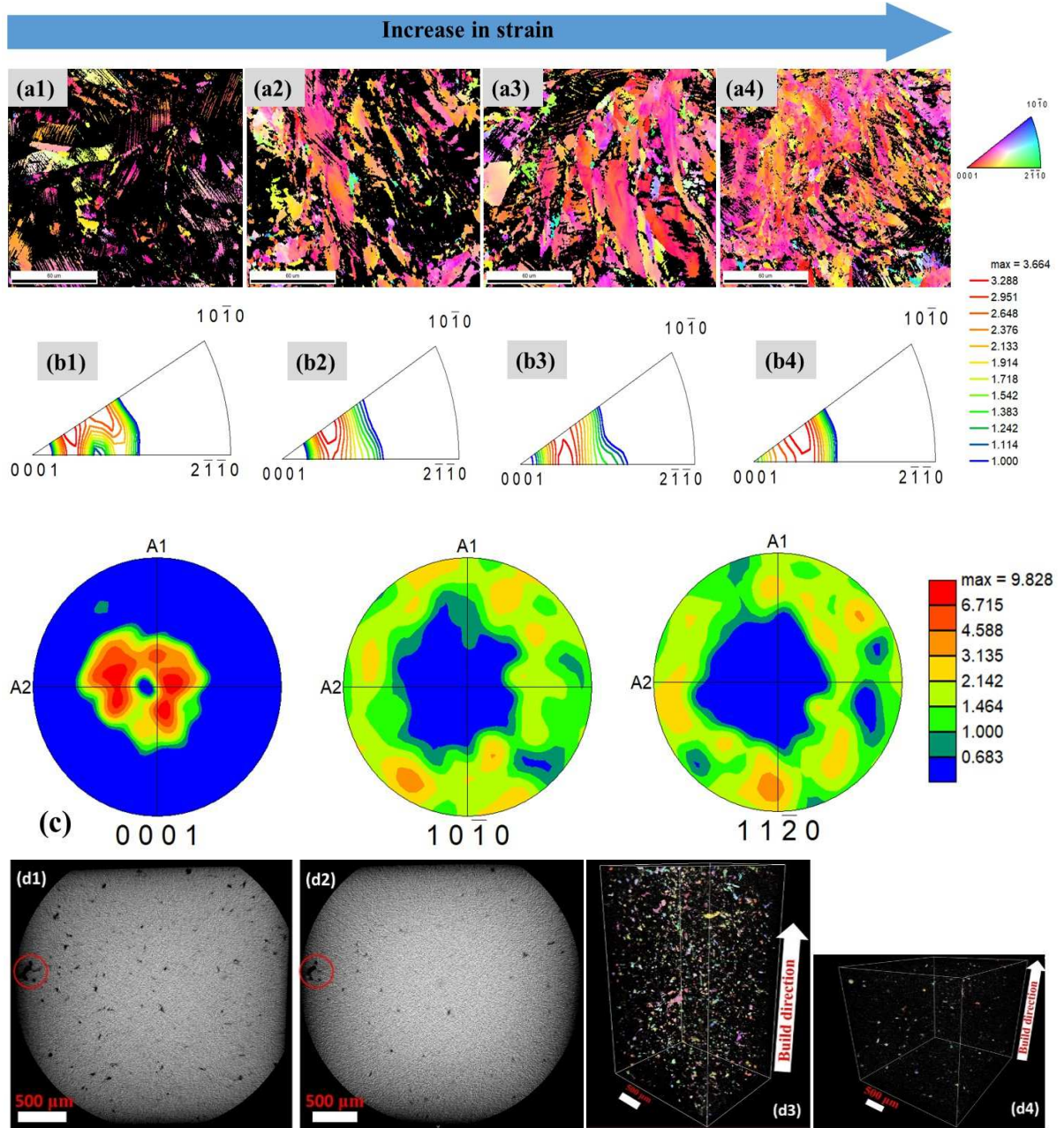


Figure 7: (a1-a4) EBSD micrographs showing IPF indicating the texture evolution in ϵ (h.c.p.) phase, (b1-b4) corresponding IPF maps showing the near basal texture evolution in the ϵ (h.c.p.) grains, (c) h.c.p. pole figure of the ϵ (h.c.p.) grains obtained on a transverse section of the specimen after compression, (d1) XRM slice depicting the internal distribution of pores in as-built Cu-HEA, (d2) corresponding XRM slice at the same section obtained after deforming to 30% strain at 10^{-3} s⁻¹ (same pore in both images is enclosed in red circles), (d3-d4) 3D reconstructed images of the cubic specimen before and after compression, respectively.

3.4 Evolution of c/a ratio associated with ϵ (h.c.p.) phase

Sinha et al. (Sinha et al., 2019) studied deformation mechanisms in the ϵ (h.c.p.) phase in TRIP

HEAs and reported that c/a ratio is dependent on alloy chemistry as well as processing and deformation conditions. Excellent strain hardening capacity of TRIP HEAs was attributed to less-than-ideal c/a ratio (1.633), which invokes the non-basal slip systems at higher strains. Further, the strain induced γ (f.c.c.) \rightarrow ϵ (h.c.p.) transformation in TRIP HEAs was accompanied by volume contraction in the ϵ (h.c.p.) phase (Sinha et al., 2019; Wei et al., 2019). Recently, Frank et al. (Frank et al., 2020) performed an in-situ neutron diffraction analysis on CS-HEA under tensile deformation and reported a decrease in c/a ratio from 1.619 to 1.588 with strain. Decrease in c/a ratio under tensile deformation was attributed to the activation of non-basal $\langle c+a \rangle$ pyramidal slip systems as well as extension and contraction twinning capable of accommodating strain along the c -axis at larger strain levels. The processing- and deformation-dependent nature of c/a ratio in TRIP HEAs motivated us to study the evolution of c/a ratio in AMed Cu-HEA under uniaxial compression. Lattice parameters for γ (f.c.c.) and ϵ (h.c.p.) phases were computed from the XRD peaks, as explained in section 2.2.3. The c/a ratio of the as-built Cu-HEA was obtained as 1.612. Figure 8 (a) illustrates the XRD data of AMed Cu-HEA for the specimens deformed at different axial strain (ε_c) levels at 10^0 s $^{-1}$, whereas, Fig. 8 (b) shows XRD data of the compression specimens at near failure/maximum strain achieved at different strain rates. XRD scanning parameters were kept constant for all scans. The relative decrease in the magnitude of γ (f.c.c.) peaks and corresponding increase in the magnitude of ϵ (h.c.p.) peaks indicate the relative increase in transformation with deformation (Fig. 8 (a)). Peak shift and peak broadening of γ (f.c.c.) peaks were observed with increase in straining that was attributed mainly to generation of stacking faults and lattice distortion (Makinson et al., 2000; Sinha et al., 2019). Figures 8(c1–c3) depict the evolution of c/a ratio and lattice parameters (c , a) of ϵ (h.c.p.) as a function of strain at three different strain rates, viz. 10^{-3} s $^{-1}$, 10^0 s $^{-1}$ and 2.5×10^3 s $^{-1}$. Clearly, the marginal increase of c/a ratio with strain at a specific strain rate under uniaxial compression (Fig. 8 (c1)) is attributed to extension along the c -axis and marginal contraction of a (Figs. 8 (c2–c3)). However, the value of c/a at all strain levels remains below the ideal c/a ratio, and signify the capability of the material to accommodate strain at large deformation by invoking the non-basal $\langle c+a \rangle$ slip modes. As phase evolution during straining influences the c/a ratio (Sinha et al., 2019), correlating Fig. 8 (c1) with Fig. 5 (d) is necessary. Although maximum strain levels were comparable for 10^{-3} s $^{-1}$ and 10^0 s $^{-1}$, percentage transformation was lower at 10^0 s $^{-1}$. Hence, stress partitioning between the two phases varies at larger strain levels (Frank et al., 2020). Evolution

of c/a ratio largely depends on the lattice strain associated with ϵ (h.c.p.) phase as well as the activation of different slip systems (Frank et al., 2020). Further, Sinha et al. (Sinha et al., 2019) reported that the final c/a ratio is also influenced by the transformed/deformed nature of ϵ (h.c.p.) phase. Work hardening in a metastable HEA with ϵ (h.c.p.) dominant initial microstructure is largely characterized by deformation of ϵ (h.c.p.) phase whereas work hardening in a γ (f.c.c.) dominant microstructure is mostly characterized by TRIP (Sinha et al., 2020). In AMed Cu-HEA, sustained transformation with strain at 10^{-3} s⁻¹ (Fig. 5 (d)) indicates that strain accommodation is characterized largely by TRIP. Hence, the lattice strain associated with ϵ (h.c.p.) phase is somewhat lower and thus resulted in lesser variation in c/a ratio with deformation; 1.613 at 10% strain to 1.618 at 45% strain (Fig. 8 (c1)). On the contrary, owing to sluggish transformation (47% ϵ (h.c.p.) at 25% strain to 55% ϵ (h.c.p.) at 45% strain) at large strain levels applied at 10^0 s⁻¹, strain accommodation in ϵ (h.c.p.) phase is chiefly by deformation of the transformed ϵ (h.c.p.) grains already present in the matrix, which strains the lattice with an extension along c -axis and marginal contraction of a (Figs. 8 (c2) and (c3)). Hence, larger variation of c/a with strain is obtained; 1.612 at 9% strain to 1.621 at 47% strain (Fig. 8 (c1)). Similar reasoning can be applied to justify the trend in c/a ratio in specimens deformed at 2.5×10^3 s⁻¹. Such variations in deformation response affect the contribution of each phase towards the final hardening. Since ϵ (h.c.p.) phase stress is higher than the γ (f.c.c.) phase stress at a specific strain level (Chen et al., 2020; Frank et al., 2020), lower ϵ (h.c.p.) phase fraction deleteriously affects the final flow stress and hardening response of the material, and justifies the lower hardening rate observed at near-dynamic and dynamic strain rates (Fig. 4 (d)). Additionally, the volume change during γ (f.c.c.) \rightarrow ϵ (h.c.p.) transformation was computed using Eq. 10 (Sinha et al., 2019) and is shown in Fig. 8 (d).

$$\Delta V = \frac{2V_{h.c.p.} - V_{f.c.c.}}{V_{f.c.c.}}. \quad (10)$$

$$V_{f.c.c.} = a_{f.c.c.}^3. \quad (11)$$

$$V_{h.c.p.} = \frac{\sqrt{3}}{2} a_{h.c.p.}^2 c_{h.c.p.}. \quad (12)$$

where $a_{f.c.c.}$ is the f.c.c. lattice parameter and $a_{h.c.p.}$ and $c_{h.c.p.}$ are the h.c.p lattice parameters. Earlier works reported a -ve ΔV during γ (f.c.c.) \rightarrow ϵ (h.c.p.) transformation in shape memory alloys (Stanford and Dunne, 2010) as well as in TRIP HEAs (Sinha et al., 2019; Wei et al., 2019). Volume change during γ (f.c.c.) \rightarrow ϵ (h.c.p.) transformation is accommodated by lattice

adjustments within the ϵ (h.c.p.) phase. In the present study too, a –ve ΔV was observed during γ (f.c.c.) \rightarrow ϵ (h.c.p.) transformation. The magnitude of volume contraction, $|\Delta V|$, decreases with an increase in compressive strain which is attributed to the relative variation of f.c.c. and h.c.p. lattice parameters. Furthermore, $|\Delta V|$ decreases with an increase in c/a ratio (Figs. 8 (c1) and (d)). Similar trend in the values of $|\Delta V|$ with c/a ratio was also reported in (Sinha et al., 2019). (*Detailed description of lattice parameters is provided in supplementary data Table T1*).

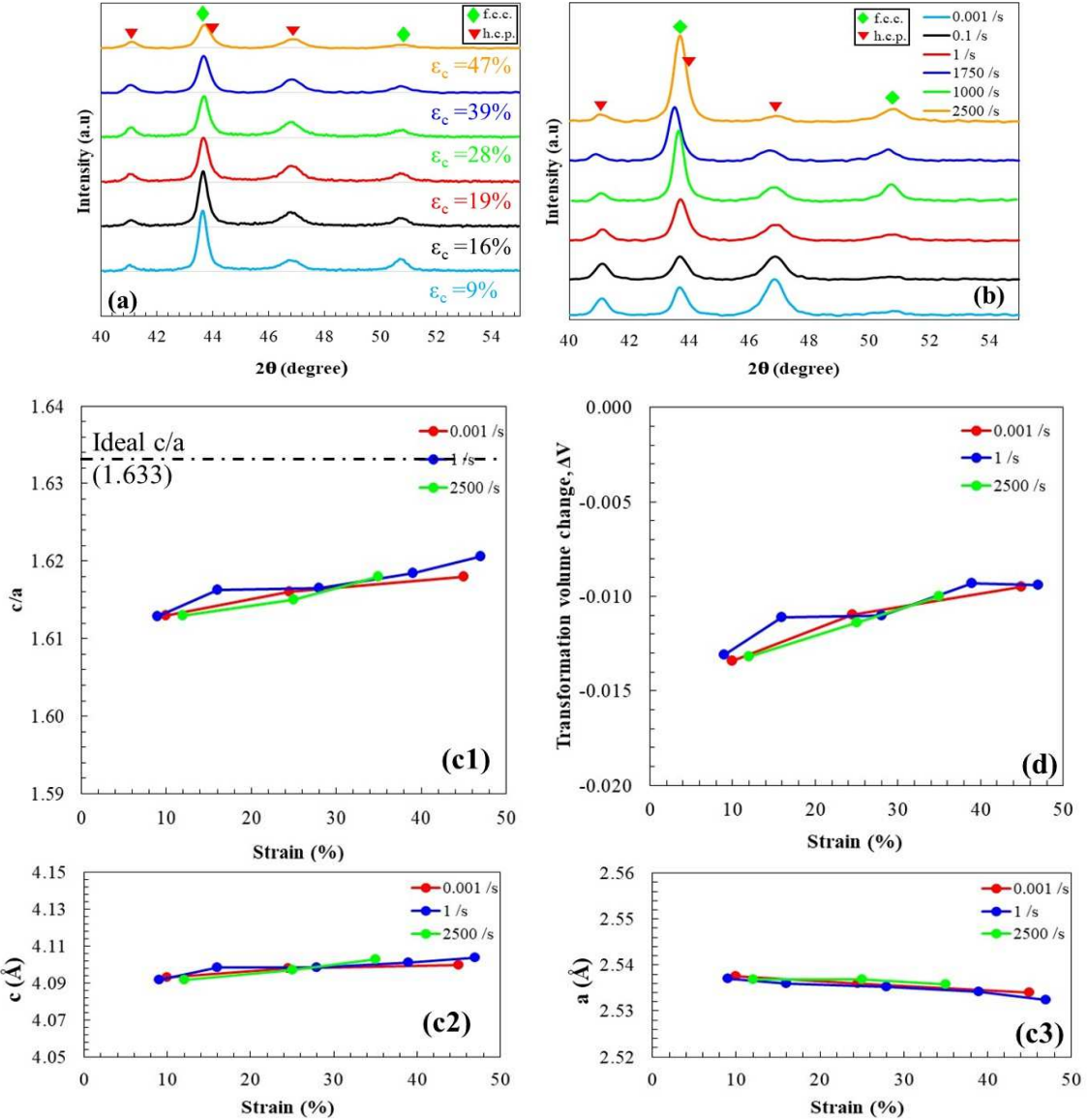


Figure 8: XRD data of (a) the compression samples tested at 10^0 s^{-1} to different strain levels, (b) compression specimens at maximum/near failure strains at different strain rates, (c1-c3) evolution of c/a ratio and lattice parameters c and a of ε (h.c.p.) phase, and (d) transformation volume change as a function of strain and strain rate during deformation.

3.5 Propensity of activation of different deformation modes in ε (h.c.p.) phase

This section is dedicated to correlating the strong near-basal texture developed in ε (h.c.p.) phase with different deformation modes invoked during deformation. Previous studies reported c/a ratio of ε (h.c.p.) in DP HEAs closer to Mg ($c/a = 1.624$), hence, kept Mg as a reference for

further analysis of the deformation modes (Bu et al., 2019; Wei et al., 2019). In Mg alloys, $\langle a \rangle$ basal slip $\{0001\} <1\bar{2}10>$ is the main strain accommodating mechanism due to its lower critical resolved shear stress (CRSS) for activation. However, non-basal slip systems such as prismatic $\{10\bar{1}0\} <\bar{1}2\bar{1}0>$, pyramidal $\langle a \rangle \{10\bar{1}1\} <\bar{1}2\bar{1}0>$, first-order pyramidal $\langle c+a \rangle \{10\bar{1}1\} <2\bar{1}\bar{1}3>$ and second-order pyramidal $\langle c+a \rangle \{2\bar{1}\bar{1}2\} <2\bar{1}\bar{1}3>$ are activated under specific conditions and contribute to higher strength and ductility. As mentioned before, strain accommodation along the c -axis is achieved by activation of non-basal $\langle c+a \rangle$ pyramidal slip as well as by extension and contraction twinning. A combination of EBSD and neutron diffraction analysis carried out on CS-HEA revealed presence of prominent twinning during tensile deformation (Frank et al., 2020; Sinha et al., 2019). Since CRSS is higher for non-basal slip systems as compared to basal slip system, their activation is suppressed at lower strain levels, where most of the plastic strain is accommodated by basal $\langle a \rangle$ slip activity when deformed in uniaxial compression (Sinha et al., 2020; Yi et al., 2006). However, the propensity of activation of different slip systems is also influenced by the initial texture along the axis of loading and vice versa (Agnew et al., 2001). The propensity of activation of various deformation modes can be understood by analyzing the Schmid factor (SF) for different slip systems. Figure 9 (a) shows the micrographs that display the SF distribution for different slip systems in compressed specimens at 10^{-3} s $^{-1}$, 10^0 s $^{-1}$ and 2.5×10^3 s $^{-1}$; Fig. 9 (b) is a pictorial representation of Fig. 9 (a). The ϵ (h.c.p.) grain orientation with a strong near-basal texture along the compression axis (Figs. 7 (a1–a4)) favors the activation of basal slip owing to its higher SF (~0.35) at all three strain rates. The propensity for prismatic slip in ϵ (h.c.p.) grains is less due to lower SF value (~0.16) (Fig. 9 (b)). As mentioned before, the loading axis being parallel to the axis of build of the AMed Cu-HEA indicates that the load was applied nearly along the c -axis of the ϵ (h.c.p.) phase due to strong near-basal texture of ϵ (h.c.p.) phase. Basal slip reorients the c -axis of the crystals towards the loading axis when deformed in uniaxial compression, and develops a strong basal texture (Chapuis and Liu, 2015). Hence, the activation of basal slip in the already strong near-basal textured grains reorients the $\{0\ 0\ 0\ 1\}$ poles towards the loading axis and results in a stronger near-basal texture with deformation (Figs. 7(b1–b4)). Apart from slip activity, hardening in TRIP HEAs is also characterized by the activation of different twin systems in ϵ (h.c.p.) phase (Frank et al., 2020). $\{10\bar{1}2\} <10\bar{1}1>$ extension twinning and both $\{10\bar{1}1\} <10\bar{1}2>$ and $\{10\bar{1}3\} <30\bar{3}2>$ compression twinning were observed in previous studies on TRIP HEAs (Frank et al.,

2020; Sinha et al., 2019). Additionally, the presence of extension twinning, marked by 86.2° misorientation angle, also facilitates c-axis rotation towards the loading axis in the initial stages of compression (Yi et al., 2006). Evidence of extension twinning was also observed in the current AMed Cu-HEA under compression (encircled by black ellipses in Figs. 9 (c1–c2)). Hence, the conclusion is that, presence of a strong near-basal texture which favor the basal slip (high SF) along with extension twinning activity reoriented the ϵ (h.c.p.) crystals towards the loading axis, and resulted in a much stronger near-basal texture after deformation (Figs. 7 (b1–b4)). At higher compressive strains, the relative activity of basal slip reduces , whereas $\langle c+a \rangle$ pyramidal slip activity increases (Sinha et al., 2020; Yi et al., 2006). The SF values shown in Fig. 9 (a) also infer that grain orientation favors $\langle c+a \rangle$ slip activity, thus assists the alloy to achieve high strength and compressive ductility (Figs. 4 (a) and (d)). Moreover, involvement of non-basal $\langle c+a \rangle$ slip activity can also be evidenced from the variation of lattice parameter 'c' with deformation (Frank et al., 2020). In AMed Cu-HEA loaded at 10^0 s $^{-1}$, larger variation in the value of 'c' from 4.0983 Å at 28 % strain to 4.1039 Å at 47% strain ($|\Delta c| = 0.0056$ Å) and relatively lesser variation in value of 'a' from 2.5352 Å at 28 % strain to 5.5338 Å at 47% strain ($|\Delta a| = 0.0014$ Å) indicate the dominance of $\langle c+a \rangle$ slip activity over basal slip at higher strain levels. Hence, the strong basal slip activity that dominated at lower axial strain levels along with the extension twinning reoriented the c-axis towards the compression loading axis, thereby resulting in a stronger near-basal texture; whereas $\langle c+a \rangle$ dislocation activity dominated at larger strains, and aided in achieving excellent hardening and ductility in the alloy under uniaxial compression.

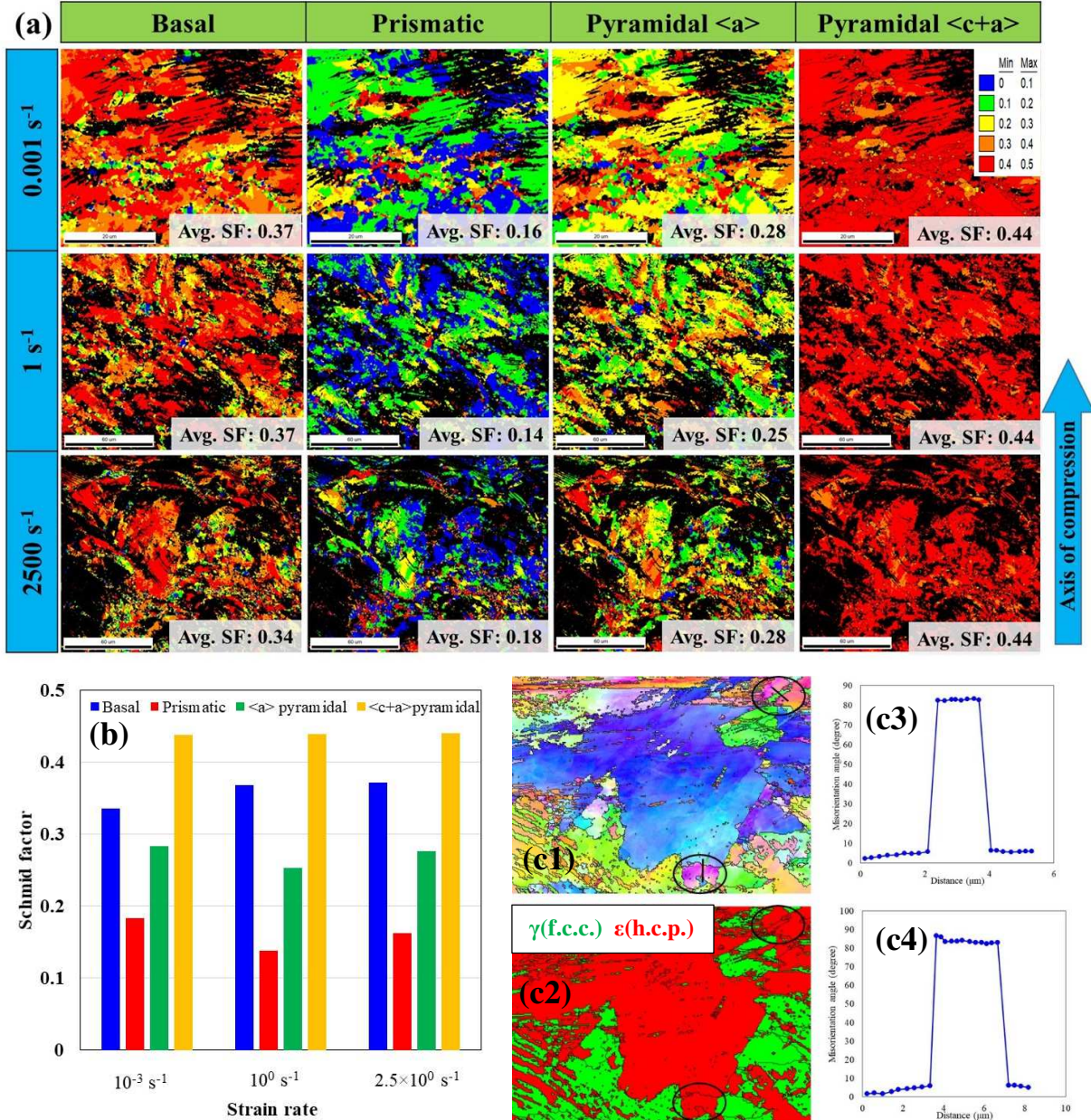


Figure 9: EBSD micrographs showing the Schmid factor distribution in the ϵ (h.c.p.) phase grain at strain rates 10^{-3} s^{-1} , 10^0 s^{-1} and $2.5 \times 10^0 \text{ s}^{-1}$, (b) pictorial representation of Schmid factor at strain rates 10^{-3} s^{-1} , 10^0 s^{-1} and $2.5 \times 10^0 \text{ s}^{-1}$, (c1) IPF map indicating the presence of extension twinning (encircled by black ellipses), (c2) corresponding phase map, and (c3-c4) misorientation across the extension twins highlighted in (c1).

3.6 Modeling of material flow behavior

Finite element modeling (FEM) requires accurate representation of material behavior as a function of strain, strain rate and temperature in the form of a constitutive equation to analyze a

wide range of problems involving high strain rate and temperature. The accuracy of FEM depends largely on how accurate the material model definition is. Several empirical (Huang and Khan, 1992; Johnson and Cook, 1985; Khan et al., 2004; Akhtar S. Khan and Liu, 2012; Khan and Zhang, 2000; Liang and Khan, 1999; Song and Sanborn, 2019; Wang et al., 2019; Zhang et al., 2015), semi-empirical (Abed and Voyatzis, 2005; Samantaray et al., 2009b; Zerilli, 2004; Zerilli and Armstrong, 1997, 1992) and physically-based models (Bammann, 1990; Bammann et al., 1990; Bammann and Aifantis, 1987; Follansbee and Kocks, 1988; Mecking and Kocks, 1981; Nemat-Nasser et al., 2001; Nemat-Nasser and Li, 1998) were applied successfully in various numerical studies. Empirical and semi-empirical models are preferred over physically-based models for structural analysis in finite element packages because fewer material constants are involved and a minimum of experiments are required to evaluate the constants.

Among the empirical models, the Johnson-Cook (JC) model (Johnson and Cook, 1985) (Eq. 13), which is present in various commercially-available FEA packages, is widely applied for a variety of materials. The three terms in Eq. 13 account for strain hardening, strain rate hardening and thermal softening, respectively. Another reason for the wide acceptance of the JC model is that it involves minimum material constants. Further, to ensure its applicability to a wide range of materials, the JC model was subjected to many modifications (Bobbili and Madhu, 2018; Lin et al., 2010; Song and Sanborn, 2019; Tan et al., 2015; Wang et al., 2019, 2013; Zhang et al., 2015; F. Zhang et al., 2020).

$$\sigma = (A + B\varepsilon^n)(1 + C\ln\dot{\varepsilon}^*)(1 - (T^*)^m), \quad (13)$$

where σ is the equivalent flow stress (von-Mises), ε is the equivalent plastic strain, A is the yield strength at reference strain rate and temperature, B is the strain hardening coefficient, n is the strain hardening exponent, C is the strain rate hardening coefficient and m is the thermal softening exponent. $\dot{\varepsilon}^* = \frac{\dot{\varepsilon}}{\dot{\varepsilon}_0}$, is the dimensionless strain rate and $T^* = \frac{(T-T_r)}{(T_m-T_r)}$, is the homologous temperature. $\dot{\varepsilon}$ and $\dot{\varepsilon}_0$ are the current and reference strain rates, respectively. T , T_r and T_m are the current, reference and melting point temperatures in absolute units, respectively.

The Zerilli-Armstrong (ZA) model (Zerilli and Armstrong, 1992) is a dislocation mechanics-based semi-empirical model that also accounts for strain hardening, strain rate hardening and thermal softening. The advantage of the ZA model over the JC model is the introduction of

coupling between temperature and strain rate on flow stress. Additionally, the ZA model accounts for the difference in rate-controlling mechanisms in F.C.C.- and B.C.C.-based alloys by providing two separate equations, as given below (Eqs. (14–15)).

$$\text{For B.C.C. metals, } \sigma = C_0 + C_1 \exp(-C_3 T + C_4 T \ln \dot{\varepsilon}) + C_5 \varepsilon^n; \quad (14)$$

$$\text{for F.C.C. metals, } \sigma = C_0 + C_2 \varepsilon^{0.5} \exp(-C_3 T + C_4 T \ln \dot{\varepsilon}), \quad (15)$$

where C_0 is the athermal component of yield stress that correlates directly with material grain size, and C_1, C_2, C_3, C_4 and C_5 are material parameters. Of extreme and special emphasis is that the dependence of flow stress on strain is independent of temperature and strain rate in B.C.C. alloys; whereas in F.C.C. alloys, the ZA model considers the strain dependence on strain rate and temperature. Later, Samantaray et al. (Samantaray et al., 2009b) proposed a modified ZA (MZA) model (Eq. 16) for F.C.C. alloys to account for the coupling effect on strain and temperature, and strain rate and temperature on flow stress (Samantaray et al., 2011, 2009a).

$$\sigma = (A_1 + A_2 \varepsilon^n) \exp\{-(A_3 + A_4 \varepsilon) \bar{T} + (A_5 + A_6 \bar{T}) \ln \dot{\varepsilon}^*\}, \quad (16)$$

where $\bar{T} = (T - T_r)$ and A_1, A_2, A_3, A_4, A_5 and A_6 are material parameters.

Another widely accepted empirical model is the Huang and Khan (KH) model (Huang and Khan, 1992) which is a modified version of the Bodner–Partom model (Bodner and Partom, 1975). Further, Khan and Liang (Liang and Khan, 1999) modified the KH model to develop the KHL model, which demonstrated applicability to B.C.C metals and alloys. The KHL model has the form as indicated in Eq. 17:

$$\sigma = \left(A + B \varepsilon^{n_0} \left(1 - \frac{\ln \dot{\varepsilon}}{\ln D_0^p} \right)^{n_1} \right) (e^{C \ln \dot{\varepsilon}}) (1 - (T^*)^m). \quad (17)$$

The KHL model considered the coupled effect of strain and strain rate on flow stress through the strain rate exponent n_1 . The second bracketed term in Eq. 17 is incorporated to include the effect of viscous drag on yield stress at high strain rates. The exponent m takes care of the thermal softening of the material at higher temperature, and n_0 is the strain hardening exponent.

The KHL model was further modified by Khan and Zhang (Khan and Zhang, 2000) to represent the behavior of materials such as nanocrystalline iron and copper mixture as well as titanium (Khan et al., 2004; Khan and Zhang, 2000). The modified KHL model is given in Eq. 18:

$$\sigma = \left(A + B \varepsilon^{n_0} \left(1 - \frac{\ln \dot{\varepsilon}}{\ln D_0^p} \right)^{n_1} \right) \left(\frac{\dot{\varepsilon}}{\dot{\varepsilon}_0} \right)^C (1 - (T^*)^m). \quad (18)$$

Recently, Khan and Liu (KL) proposed an empirical constitutive model based on the KHL model to account for strain rate sensitivity and thermal softening in AA 2024-T351 (Akhtar S Khan and Liu, 2012). The model is represented in Eq. 19.

$$\sigma = \left[A + B \varepsilon^{n_0} e^{-C_3 \frac{\dot{\varepsilon}}{\dot{\varepsilon}_0} \left(\frac{T_m - T}{T_m - T_r} \right)^{m_1}} \right] \left[e^{C_1 \frac{\dot{\varepsilon}}{\dot{\varepsilon}_0}} - C_2(T) e^{-K_1 \dot{\varepsilon}} \right] \left[\frac{T_m - T}{T_m - T_r} \right]^{m_2}, \quad (19)$$

$$\text{where } C_2(T) = \left[\frac{1}{2} \frac{(T - T_c) + |T - T_c|}{(T_m - T_r)} \right]^{m_3}. \quad (20)$$

In Eq. 19, constant C_3 and exponent m_1 describe the decrease in work hardening with increase in strain rate and temperature, respectively. Constant C_1 defines the viscous drag effect on flow stress at high strain rates. $C_2(T)$ and constant K_1 characterize the effect of temperature and strain rate on strain rate sensitivity at temperatures above the threshold temperature T_c .

As presented in sections 3.2 and 3.3, the work hardening of Cu-HEA at different strain rates is governed by the rate of γ (f.c.c.) \rightarrow ε (h.c.p.) transformation, work hardening rate being higher at quasi-static strain rates and lower at dynamic strain rates. The JC model (Eq.13), the MZA model (Eq. 16), the modified KHL model (Eq. 18), and the KL model (Eq. 19) have been applied to the present TRIP Cu-HEA to analyze the effectiveness of each model to characterize the strain-rate sensitive flow behavior at room temperature (T_r). Possible thermal softening of the material at higher temperature is not considered for curve fitting of the models due to lack of high temperature data available. Also, the influence of adiabatic heating on mechanical response of the alloy is assumed to be negligible. Hence, the temperature dependency on flow stress is not considered in the following analysis due to which the thermal softening coefficients and exponents in Eqns. 13, 16, 18, and 19 are assumed to be zero. The experimental results at different strain rates at room temperature (T_r) obtained from MTS and SHPB were used to determine the model constants in each case. The reference strain rate, $\dot{\varepsilon}_0$, is considered as 10^{-3} s $^{-1}$. The material parameters for the JC, MZA, modified KHL and KL models are determined by following the steps described in (Lin et al., 2010), (Samantaray et al., 2009b), (Khan and Zhang, 2000) and (Akhtar S Khan and Liu, 2012) and are given in Tables 3–6, respectively.

Table 3: JC model material constants obtained for TRIP Cu-HEA

A (MPa)	B (MPa)	n	C
---------	---------	---	---

510	1380	0.63	0.011
-----	------	------	-------

Table 4: MZA model material constants obtained for TRIP Cu-HEA

A ₁ (MPa)	A ₂ (MPa)	n	A ₅
510	1380	0.63	0.0125

Table 5: Modified KHL model parameters for TRIP Cu-HEA

A (MPa)	B (MPa)	n ₀	n ₁	C
510	1380	0.63	0.17	0.0125

Table 6: KL model material parameters for TRIP Cu-HEA

A (MPa)	B (MPa)	n ₀	C ₃	C ₁
510	1380	0.63	2.1E-7	1.7e-7

Figures 10 (a)–(d) depict the correlation of experimental results with the predictions from the JC, MZA, Modified KHL, and KL models, respectively. The JC model could predict material flow behavior reasonably well at low strain rate regime (10^{-3} s⁻¹ – 10^0 s⁻¹), whereas at higher strain rates (10^3 s⁻¹ – 2.5×10^3 s⁻¹), the model failed to predict flow behavior accurately (Fig. 10 (a)). The higher strain rate sensitivity indicated by the material at high strain rates ($m = 0.18$ in Fig. 4 (c)) was not captured perfectly by the JC model. The term $(1 + C \ln \dot{\epsilon}^*)$ in Eq. 13 is not sufficient to capture the viscous drag effect of the material at strain rates greater than 10^3 s⁻¹. Similar to the JC model, the MZA model was also incapable of predicting high strain rate material flow response. However, at lower strain rates (10^{-3} s⁻¹ – 10^0 s⁻¹), model prediction indicated satisfactory agreement with experimental results (Fig. 10 (b)). Additionally, the MZA model over-predicted the rate of hardening at high strain rates (evident from the difference in slope of the stress-strain response of the model predictions and experiments). This over-prediction is due to the fact that the MZA model (Eq. 16) lacks a term that accounts for the reduction in hardening with strain at higher strain rates. The Modified KHL model (Eq. 18) over-predicted flow behavior at low strain rates, whereas it under-predicted material flow response at high strain rates (Fig. 10 (c)). However, inclusion of the term $\left(1 - \frac{\ln \dot{\epsilon}}{\ln D_0^p}\right)^{n_1}$, which accounts for the reduction in

hardening rate at high strain rates, yielded a better trend to the true stress-strain response curve in terms of hardening when compared to the MZA model. Finally, the correlation of the KL model with experimental results was analyzed (Fig. 10 (d)). The model could well correlate experimental results at high strain rates when compared to the other three models. The KL model could model the viscous drag effect successfully as well as the reduction in material hardening due to lower transformation levels at high strain rates. Additionally, KL model prediction indicated reasonable agreement with experimental results at lower strain rates, although rate sensitivity is negligible within a strain rate range of $10^{-3} \text{ s}^{-1} - 10^0 \text{ s}^{-1}$. Comparing all four models, the KL model could better capture the variation in flow behavior due to variation in transformation in the current TRIP Cu-HEA at strain rates varying from $10^{-3} \text{ s}^{-1} - 2.5 \times 10^3 \text{ s}^{-1}$.

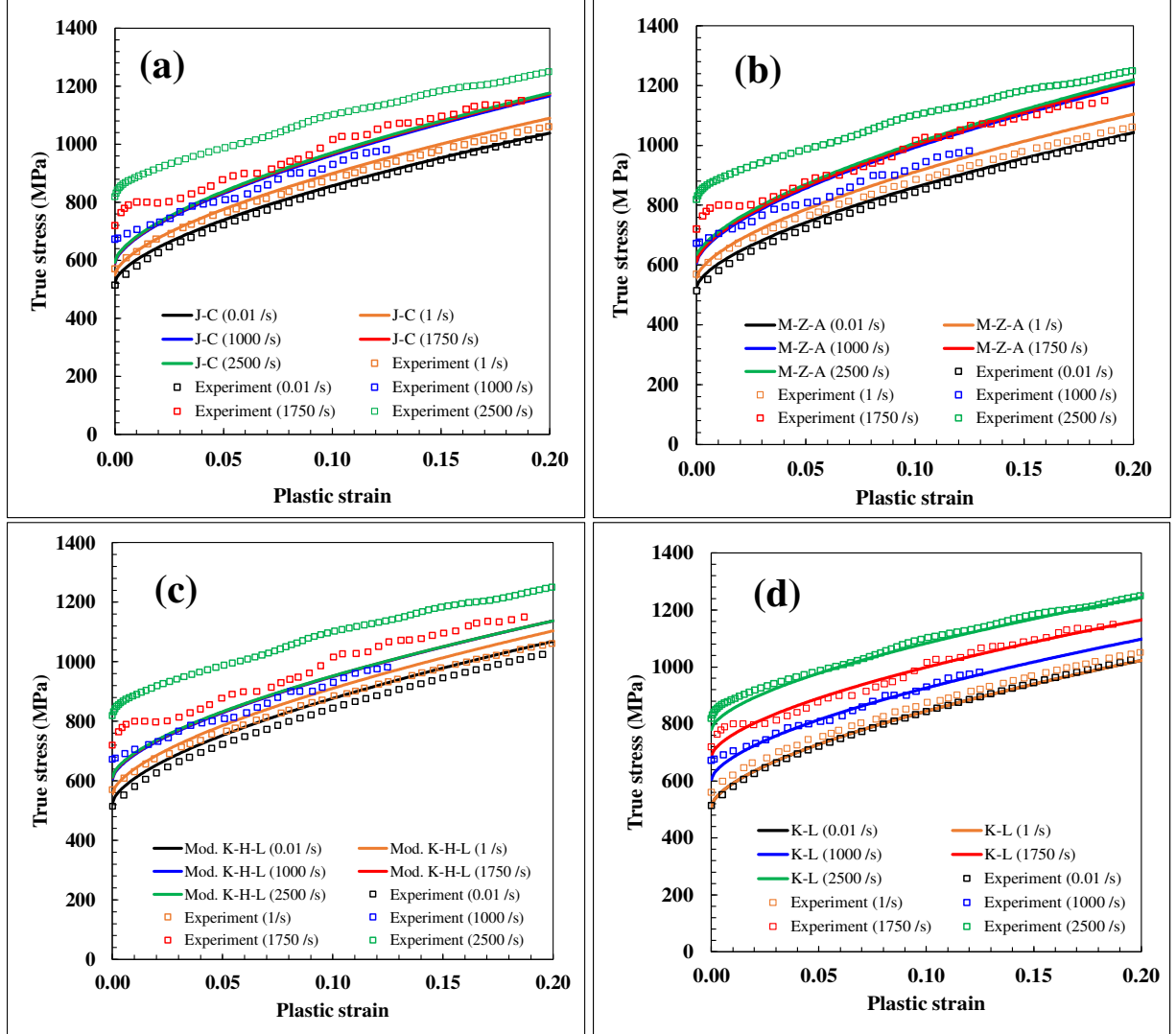


Figure 10: Correlations of different empirical models with the experimental results of TRIP Cu-HEA at multiple strain rates (a) JC model, (b) MZA model, (c) modified KHL model, and (d) KL model.

4 Conclusions

Quasi-static, medium and high strain rate compression response and microstructural evolution in a LPBF made DP TRIP Cu-HEA were investigated. The alloy displayed excellent work hardening with value of ultimate strength reaching ~ 1.4 GPa (true stress) at different strain rates. Important conclusions of the current study are summarized below.

1. Excellent strength and work hardening capability of AMed DP Cu-HEA are attributed

mainly to the strain-induced γ (f.c.c.) \rightarrow ϵ (h.c.p.) transformation in the γ (f.c.c.) dominant as-built microstructure.

2. The alloy exhibited high strain rate sensitivity from strain rates varying from 10^{-3} s $^{-1}$ to 2.5×10^{-3} s $^{-1}$. Of special emphasis is the negative rate sensitivity that was observed at a strain rate of 10^0 s $^{-1}$ compared to the quasi-static mechanical response. Sluggish transformation kinetics and thermal softening due to adiabatic heating reduced the work hardening rate in the alloy at near-dynamic and dynamic strain rates.
3. Transformation of γ (f.c.c.) phase with a dominant dual texture along the axis of compression in the as-built microstructure, oriented towards {1 1 1} and {1 0 1}, resulted in a strong {0 0 0 1} near-basal texture in the ϵ (h.c.p.) phase, well complied with S-N OR.
4. Less than ideal c/a ratio identified in the ϵ (h.c.p.) phase indicated a marginal increase with strain, varying from 1.612 to 1.622. Phase evolution, transformed- and/or deformed-nature of the ϵ (h.c.p.) phase, lattice strain associated with ϵ (h.c.p.) phase are the factors that govern the evolution of c/a ratio.
5. Basal slip activity in the initial phase of loading along with extension twinning reoriented the c -axis of ϵ (h.c.p.) phase crystals towards the compression loading axis and resulted in a stronger near-basal texture with compression, whereas excellent hardening and ductility were attributed to dominant $\langle c+a \rangle$ pyramidal slip activity invoked at larger strain levels.
6. Among existing empirical constitutive models, the KL model could better capture the strain rate sensitive response of Cu-HEA when compared to other renowned models such as the JC model, the MZA model and the KHL model.

Acknowledgments

The present study was conducted under the co-operative agreement between Army Research Laboratory, USA and University of North Texas (W911NF1920011). Authors acknowledge Materials Research Facility at University of North Texas for access to scanning electron microscopy and X-ray diffraction facility as well as Advanced Materials and Manufacturing Processes Institute at University of North Texas for access to X-ray microscopy. Authors thank Haider Janjua and Christopher Morphew for helping with precise polishing of the specimens.

Authorship contribution statement

Ravi Sankar Haridas: Conceptualization, Data curation, Formal analysis, Methodology, Writing - Original draft. **Priyanshi Agrawal:** Methodology, Formal analysis, Writing - review & editing. **Saket Thapliyal:** Conceptualization, Methodology, Formal analysis, Writing - review & editing. **Surekha Yadav:** Methodology, Formal analysis, Writing - review & editing. **Rajiv S. Mishra:** Conceptualization, Project administration, Resources, Supervision, Writing - review & editing. **Brandon A. McWilliams:** Project administration, Writing - review & editing. **Kyu C. Cho:** Project administration, Writing - review & editing.

References

- Abed, F.H., Voyatzis, G.Z., 2005. A consistent modified Zerilli-Armstrong flow stress model for BCC and FCC metals for elevated temperatures. *Acta Mech.* 175, 1–18. <https://doi.org/10.1007/s00707-004-0203-1>
- Agnew, S.R., Yoo, M.H., Tomé, C.N., 2001. Application of texture simulation to understanding mechanical behavior of Mg and solid solution alloys containing Li or Y. *Acta Mater.* 49, 4277–4289. [https://doi.org/10.1016/S1359-6454\(01\)00297-X](https://doi.org/10.1016/S1359-6454(01)00297-X)
- Agrawal, P., Thapliyal, S., Nene, S.S., Mishra, R.S., McWilliams, B.A., Cho, K.C., 2020. Excellent strength-ductility synergy in metastable high entropy alloy by laser powder bed additive manufacturing. *Addit. Manuf.* 32, 101098. <https://doi.org/10.1016/J.ADDMA.2020.101098>
- Bammann, D.J., 1990. Modeling temperature and strain rate dependent large deformations of metals. *Appl. Mech. Rev.* 43, 312–319.
- Bammann, D.J., Aifantis, E.C., 1987. A model for finite-deformation plasticity. *Acta Mech.* 69, 97–117. <https://doi.org/10.1007/BF01175716>
- Bammann, D.J., Johnson, G.C., Chiesa, M.L., 1990. A strain rate dependent flow surface model of plasticity. SAND90-8227.
- Basu, S., Li, Z., Pradeep, K.G., Raabe, D., 2018. Strain rate sensitivity of a TRIP-assisted dual-phase high-entropy alloy. *Front. Mater.* 5, 1–10. <https://doi.org/10.3389/fmats.2018.00030>
- Bhattacharyya, J.J., Agnew, S.R., Lee, M.M., Whittington, W.R., El Kadiri, H., 2017. Measuring and modeling the anisotropic, high strain rate deformation of Al alloy, 7085, plate in T711 temper. *Int. J. Plast.* 93, 46–63. <https://doi.org/10.1016/j.ijplas.2017.03.001>
- Bobbili, R., Madhu, V., 2018. A modified Johnson-Cook model for FeCoNiCr high entropy alloy over a wide range of strain rates. *Mater. Lett.* 218, 103–105. <https://doi.org/https://doi.org/10.1016/j.matlet.2018.01.163>
- Bodner, Sr., Partom, Y., 1975. Constitutive equations for elastic-viscoplastic strain-hardening

materials.

- Brif, Y., Thomas, M., Todd, I., 2015. The use of high-entropy alloys in additive manufacturing. *Scr. Mater.* 99, 93–96. <https://doi.org/10.1016/j.scriptamat.2014.11.037>
- Bu, Y., Li, Z., Liu, J., Wang, H., Raabe, D., Yang, W., 2019. Nonbasal Slip Systems Enable a Strong and Ductile Hexagonal-Close-Packed High-Entropy Phase. *Phys. Rev. Lett.* 122, 75502. <https://doi.org/10.1103/PhysRevLett.122.075502>
- Chapuis, A., Liu, Q., 2015. Simulations of texture evolution for HCP metals: Influence of the main slip systems. *Comput. Mater. Sci.* 97, 121–126. <https://doi.org/10.1016/J.COMMATSCL.2014.10.017>
- Chen, S., Oh, H.S., Gludovatz, B., Kim, S.J., Park, E.S., Zhang, Z., Ritchie, R.O., Yu, Q., 2020. Real-time observations of TRIP-induced ultrahigh strain hardening in a dual-phase CrMnFeCoNi high-entropy alloy. *Nat. Commun.* 11, 1–8. <https://doi.org/10.1038/s41467-020-14641-1>
- Chen, W., Zhang, B., Forrestal, M.J., 1999. A Split Hopkinson Bar Technique for Low Impedance Materials. *Exp. Mech.* 39, 81–85. <https://doi.org/10.1007/BF02331109>
- Chuang, M.-H., Tsai, M.-H., Wang, W.-R., Lin, S.-J., Yeh, J.-W., 2011. Microstructure and wear behavior of Al_xCo1.5CrFeNi1.5Ti_y high-entropy alloys. *Acta Mater.* 59, 6308–6317. <https://doi.org/10.1016/J.ACTAMAT.2011.06.041>
- DebRoy, T., Wei, H.L., Zuback, J.S., Mukherjee, T., Elmer, J.W., Milewski, J.O., Beese, A.M., Wilson-Heid, A., De, A., Zhang, W., 2018. Additive manufacturing of metallic components – Process, structure and properties. *Prog. Mater. Sci.* 92, 112–224. <https://doi.org/10.1016/J.PMATSCL.2017.10.001>
- Ding, Q., Zhang, Y., Chen, X., Fu, X., Chen, D., Chen, S., Gu, L., Wei, F., Bei, H., Gao, Y., Wen, M., Li, J., Zhang, Z., Zhu, T., Ritchie, R.O., Yu, Q., 2019. Tuning element distribution, structure and properties by composition in high-entropy alloys. *Nature* 574, 223–227. <https://doi.org/10.1038/s41586-019-1617-1>
- Follansbee, P.S., Kocks, U.F., 1988. A constitutive description of the deformation of copper based on the use of the mechanical threshold stress as an internal state variable. *Acta Metall.* 36, 81–93. [https://doi.org/https://doi.org/10.1016/0001-6160\(88\)90030-2](https://doi.org/https://doi.org/10.1016/0001-6160(88)90030-2)
- Frank, M., Chen, Y., Nene, S.S., Sinha, S., Liu, K., An, K., Mishra, R.S., 2020. Investigating the deformation mechanisms of a highly metastable high entropy alloy using in-situ neutron diffraction. *Mater. Today Commun.* 23, 100858. <https://doi.org/10.1016/J.MTCOMM.2019.100858>
- Fujieda, T., Shiratori, H., Kuwabara, K., Kato, T., Yamanaka, K., Koizumi, Y., Chiba, A., 2015. First demonstration of promising selective electron beam melting method for utilizing high-entropy alloys as engineering materials. *Mater. Lett.* 159, 12–15. <https://doi.org/10.1016/j.matlet.2015.06.046>
- Gama, B.A., Lopatnikov, S.L., Gillespie, J.W., 2004. Hopkinson bar experimental technique: A critical review. *Appl. Mech. Rev.* 57, 223. <https://doi.org/10.1115/1.1704626>

- Gangireddy, S., Gwalani, B., Mishra, R.S., 2018a. Grain size dependence of strain rate sensitivity in a single phase FCC high entropy alloy Al0.3CoCrFeNi. *Mater. Sci. Eng. A* 736, 344–348. <https://doi.org/10.1016/j.msea.2018.09.009>
- Gangireddy, S., Kaimiao, L., Gwalani, B., Mishra, R., 2018b. Microstructural dependence of strain rate sensitivity in thermomechanically processed Al0.1CoCrFeNi high entropy alloy. *Mater. Sci. Eng. A* 727, 148–159. <https://doi.org/10.1016/j.msea.2018.04.108>
- Gao, T.J., Zhao, D., Zhang, T.W., Jin, T., Ma, S.G., Wang, Z.H., 2020. Strain-rate-sensitive mechanical response, twinning, and texture features of NiCoCrFe high-entropy alloy: Experiments, multi-level crystal plasticity and artificial neural networks modeling. *J. Alloys Compd.* 845. <https://doi.org/10.1016/j.jallcom.2020.155911>
- Gludovatz, B., Hohenwarter, A., Catoor, D., Chang, E.H., George, E.P., Ritchie, R.O., 2014. A fracture-resistant high-entropy alloy for cryogenic applications. *Science* (80-.). 345, 1153–1158. <https://doi.org/10.1126/science.1254581>
- Gludovatz, B., Hohenwarter, A., Thurston, K.V.S., Bei, H., Wu, Z., George, E.P., Ritchie, R.O., 2016. Exceptional damage-tolerance of a medium-entropy alloy CrCoNi at cryogenic temperatures. *Nat. Commun.* 7, 10602. <https://doi.org/10.1038/ncomms10602>
- Guo, J., Goh, M., Zhu, Z., Lee, X., Nai, M.L.S., Wei, J., 2018. On the machining of selective laser melting CoCrFeMnNi high-entropy alloy. *Mater. Des.* 153, 211–220. <https://doi.org/10.1016/j.matdes.2018.05.012>
- Haase, C., Tang, F., Wilms, M.B., Weisheit, A., Hallstedt, B., 2017. Combining thermodynamic modeling and 3D printing of elemental powder blends for high-throughput investigation of high-entropy alloys – Towards rapid alloy screening and design. *Mater. Sci. Eng. A* 688, 180–189. <https://doi.org/10.1016/j.msea.2017.01.099>
- Hrabe, N., Gnäupel-Herold, T., Quinn, T., 2017. Fatigue properties of a titanium alloy (Ti–6Al–4V) fabricated via electron beam melting (EBM): Effects of internal defects and residual stress. *Int. J. Fatigue* 94, 202–210. <https://doi.org/10.1016/j.ijfatigue.2016.04.022>
- Huang, S., Khan, A.S., 1992. Modeling the mechanical behaviour of 1100-0 aluminum at different strain rates by the bodner-partom model. *Int. J. Plast.* 8, 501–517. [https://doi.org/10.1016/0749-6419\(92\)90028-B](https://doi.org/10.1016/0749-6419(92)90028-B)
- Huo, W., Zhou, H., Fang, F., Hu, X., Xie, Z., Jiang, J., 2017. Strain-rate effect upon the tensile behavior of CoCrFeNi high-entropy alloys. *Mater. Sci. Eng. A* 689, 366–369. <https://doi.org/10.1016/j.msea.2017.02.077>
- Johnson, G.R., Cook, W.H., 1985. Fracture characteristics of three metals subjected to various strains, strain rates, temperatures and pressures. *Eng. Fract. Mech.* 21, 31–48. [https://doi.org/https://doi.org/10.1016/0013-7944\(85\)90052-9](https://doi.org/https://doi.org/10.1016/0013-7944(85)90052-9)
- Joseph, J., Stanford, N., Hodgson, P., Fabijanic, D.M., 2017. Tension/compression asymmetry in additive manufactured face centered cubic high entropy alloy. *Scr. Mater.* 129, 30–34. <https://doi.org/10.1016/j.scriptamat.2016.10.023>
- Karthik, G.M., Panikar, S., Ram, G.D.J., Kottada, R.S., 2017. Additive manufacturing of an aluminum matrix composite reinforced with nanocrystalline high-entropy alloy particles.

- Mater. Sci. Eng. A 679, 193–203. <https://doi.org/10.1016/j.msea.2016.10.038>
- Kasperovich, G., Hausmann, J., 2015. Improvement of fatigue resistance and ductility of TiAl6V4 processed by selective laser melting. J. Mater. Process. Technol. 220, 202–214. <https://doi.org/10.1016/J.JMATPROTEC.2015.01.025>
- Khan, A.S., Liu, H., 2012. Variable strain rate sensitivity in an aluminum alloy: Response and constitutive modeling. Int. J. Plast. 36, 1–14. <https://doi.org/10.1016/j.ijplas.2012.02.001>
- Khan, A.S., Liu, H., 2012. Strain rate and temperature dependent fracture criteria for isotropic and anisotropic metals. Int. J. Plast. 37, 1–15. <https://doi.org/https://doi.org/10.1016/j.ijplas.2012.01.012>
- Khan, A.S., Sung Suh, Y., Kazmi, R., 2004. Quasi-static and dynamic loading responses and constitutive modeling of titanium alloys. Int. J. Plast. 20, 2233–2248. <https://doi.org/10.1016/j.ijplas.2003.06.005>
- Khan, A.S., Zhang, H., 2000. Mechanically alloyed nanocrystalline iron and copper mixture: Behavior and constitutive modeling over a wide range of strain rates. Int. J. Plast. 16, 1477–1492. [https://doi.org/10.1016/S0749-6419\(00\)00024-3](https://doi.org/10.1016/S0749-6419(00)00024-3)
- Kurz, W., Fisher, D.J., 1998. Fundamentals of Solidification. Trans Tech Publications. <https://doi.org/10.4028/www.scientific.net/RC.35>
- Kuwabara, K., Shiratori, H., Fujieda, T., Yamanaka, K., Koizumi, Y., Chiba, A., 2018. Mechanical and corrosion properties of AlCoCrFeNi high-entropy alloy fabricated with selective electron beam melting. Addit. Manuf. 23, 264–271. <https://doi.org/10.1016/j.addma.2018.06.006>
- Leuders, S., Thöne, M., Riemer, A., Niendorf, T., Tröster, T., Richard, H.A., Maier, H.J., 2013. On the mechanical behaviour of titanium alloy TiAl6V4 manufactured by selective laser melting: Fatigue resistance and crack growth performance. Int. J. Fatigue 48, 300–307. <https://doi.org/10.1016/J.IJFATIGUE.2012.11.011>
- Li, J., Craeghs, W., Jing, C., Gong, S., Shan, F., 2017. Microstructure and physical performance of laser-induction nanocrystals modified high-entropy alloy composites on titanium alloy. Mater. Des. 117, 363–370. <https://doi.org/10.1016/j.matdes.2016.12.007>
- Li, R., Niu, P., Yuan, T., Cao, P., Chen, C., Zhou, K., 2018. Selective laser melting of an equiatomic CoCrFeMnNi high-entropy alloy: Processability, non-equilibrium microstructure and mechanical property. J. Alloys Compd. 746, 125–134. <https://doi.org/10.1016/j.jallcom.2018.02.298>
- Li, Z., Pradeep, K.G., Deng, Y., Raabe, D., Tasan, C.C., 2016. Metastable high-entropy dual-phase alloys overcome the strength–ductility trade-off. Nature 534, 227–230. <https://doi.org/10.1038/nature17981>
- Li, Z., Voisin, T., McKeown, J.T., Ye, J., Braun, T., Kamath, C., King, W.E., Wang, Y.M., 2019. Tensile properties, strain rate sensitivity, and activation volume of additively manufactured 316L stainless steels. Int. J. Plast. 120, 395–410. <https://doi.org/10.1016/j.ijplas.2019.05.009>

- Li, Z., Zhao, S., Ritchie, R.O., Meyers, M.A., 2019. Mechanical properties of high-entropy alloys with emphasis on face-centered cubic alloys. *Prog. Mater. Sci.* 102, 296–345. <https://doi.org/10.1016/j.pmatsci.2018.12.003>
- Liang, R., Khan, A.S., 1999. A critical review of experimental results and constitutive models for BCC and FCC metals over a wide range of strain rates and temperatures. *Int. J. Plast.* 15, 963–980. [https://doi.org/10.1016/S0749-6419\(99\)00021-2](https://doi.org/10.1016/S0749-6419(99)00021-2)
- Lin, Y.C., Chen, X.-M., Liu, G., 2010. A modified Johnson–Cook model for tensile behaviors of typical high-strength alloy steel. *Mater. Sci. Eng. A* 527, 6980–6986. <https://doi.org/https://doi.org/10.1016/j.msea.2010.07.061>
- Liu, K., Nene, S.S., Frank, M., Sinha, S., Mishra, R.S., 2019. Extremely high fatigue resistance in an ultrafine grained high entropy alloy. *Appl. Mater. Today* 15, 525–530. <https://doi.org/10.1016/J.APMT.2019.04.001>
- Liu, K., Nene, S.S., Frank, M., Sinha, S., Mishra, R.S., 2018. Metastability-assisted fatigue behavior in a friction stir processed dual-phase high entropy alloy. *Mater. Res. Lett.* 6, 613–619. <https://doi.org/10.1080/21663831.2018.1523240>
- Liu, W.H., Wu, Y., He, J.Y., Nieh, T.G., Lu, Z.P., 2013. Grain growth and the Hall–Petch relationship in a high-entropy FeCrNiCoMn alloy. *Scr. Mater.* 68, 526–529. <https://doi.org/10.1016/j.scriptamat.2012.12.002>
- Ma, S.G., Jiao, Z.M., Qiao, J.W., Yang, H.J., Zhang, Y., Wang, Z.H., 2016. Strain rate effects on the dynamic mechanical properties of the AlCrCuFeNi₂ high-entropy alloy. *Mater. Sci. Eng. A* 649, 35–38. <https://doi.org/10.1016/j.msea.2015.09.089>
- Madivala, M., Schwedt, A., Prahls, U., Bleck, W., 2019. Anisotropy and strain rate effects on the failure behavior of TWIP steel: A multiscale experimental study. *Int. J. Plast.* 115, 178–199. <https://doi.org/10.1016/j.ijplas.2018.11.015>
- Maity, T., Prashanth, K.G., Balci, Kim, J.T., Schöberl, T., Wang, Z., Eckert, J., 2018. Influence of severe straining and strain rate on the evolution of dislocation structures during micro-/nanoindentation in high entropy lamellar eutectics. *Int. J. Plast.* 109, 121–136. <https://doi.org/10.1016/j.ijplas.2018.05.012>
- Makinson, J.D., Lee, J.S., Magner, S.H., De Angelis, R.J., Weins, W.N., Hieronymus, a. S., 2000. X-ray diffraction signatures of defects in nanocrystalline materials. *Adv. X-ray Anal.* 42, 407–411.
- Mecking, H., Kocks, U.F., 1981. Kinetics of flow and strain-hardening. *Acta Metall.* 29, 1865–1875. [https://doi.org/https://doi.org/10.1016/0001-6160\(81\)90112-7](https://doi.org/https://doi.org/10.1016/0001-6160(81)90112-7)
- Miracle, D.B., Senkov, O.N., 2017. A critical review of high entropy alloys and related concepts. *Acta Mater.* 122, 448–511. <https://doi.org/10.1016/J.ACTAMAT.2016.08.081>
- Nemat-Nasser, S., Guo, W.-G., Nesterenko, V.F., Indrakanti, S.S., Gu, Y.-B., 2001. Dynamic response of conventional and hot isostatically pressed Ti–6Al–4V alloys: experiments and modeling. *Mech. Mater.* 33, 425–439. [https://doi.org/https://doi.org/10.1016/S0167-6636\(01\)00063-1](https://doi.org/https://doi.org/10.1016/S0167-6636(01)00063-1)

- Nemat-Nasser, S., Li, Y., 1998. Flow stress of fcc polycrystals with application to OFHC Cu. *Acta Mater.* 46, 565–577.
- Nene, S.S., Frank, M., Liu, K., Mishra, R.S., McWilliams, B.A., Cho, K.C., 2018. Extremely high strength and work hardening ability in a metastable high entropy alloy. *Sci. Rep.* 8, 9920. <https://doi.org/10.1038/s41598-018-28383-0>
- Nene, S.S., Frank, M., Liu, K., Sinha, S., Mishra, R.S., McWilliams, B.A., Cho, K.C., 2019. Corrosion-resistant high entropy alloy with high strength and ductility. *Scr. Mater.* 166, 168–172. <https://doi.org/10.1016/J.SCRIPTAMAT.2019.03.028>
- Nene, S.S., Frank, M., Liu, K., Sinha, S., Mishra, R.S., McWilliams, B., Cho, K.C., 2018a. Reversed strength-ductility relationship in microstructurally flexible high entropy alloy. *Scr. Mater.* 154, 163–167. <https://doi.org/10.1016/J.SCRIPTAMAT.2018.05.043>
- Nene, S.S., Sinha, S., Frank, M., Liu, K., Mishra, R.S., McWilliams, B.A., Cho, K.C., 2018b. Unexpected strength-ductility response in an annealed, metastable, high-entropy alloy. *Appl. Mater. Today* 13, 198–206. <https://doi.org/10.1016/J.APMT.2018.09.002>
- Ngo, T.D., Kashani, A., Imbalzano, G., Nguyen, K.T.Q., Hui, D., 2018. Additive manufacturing (3D printing): A review of materials, methods, applications and challenges. *Compos. Part B Eng.* 143, 172–196. <https://doi.org/10.1016/j.compositesb.2018.02.012>
- Nishiyama, Z., 1978. Martensitic Transformation. In Materials Science Series (eds Fine, M. E., Meshii, M. & Waymann, C. M.). Acad. Press 14–134.
- Pandey, A., Kabirian, F., Hwang, J.H., Choi, S.H., Khan, A.S., 2015. Mechanical responses and deformation mechanisms of an AZ31 Mg alloy sheet under dynamic and simple shear deformations. *Int. J. Plast.* 68, 111–131. <https://doi.org/10.1016/j.ijplas.2014.12.001>
- Pandya, K.S., Roth, C.C., Mohr, D., 2020. Strain rate and temperature dependent fracture of aluminum alloy 7075: Experiments and neural network modeling. *Int. J. Plast.* 135, 102788. <https://doi.org/10.1016/j.ijplas.2020.102788>
- Park, J.M., Moon, J., Bae, J.W., Jang, M.J., Park, J., Lee, S., Kim, H.S., 2018. Strain rate effects of dynamic compressive deformation on mechanical properties and microstructure of CoCrFeMnNi high-entropy alloy. *Mater. Sci. Eng. A* 719, 155–163. <https://doi.org/10.1016/j.msea.2018.02.031>
- Qiu, X.-W., Zhang, Y.-P., He, L., Liu, C., 2013. Microstructure and corrosion resistance of AlCrFeCuCo high entropy alloy. *J. Alloys Compd.* 549, 195–199. <https://doi.org/10.1016/J.JALLOCOM.2012.09.091>
- Rappaz, M., Blank, E., 1986. Simulation of oriented dendritic microstructures using the concept of dendritic lattice. *J. Cryst. Growth* 74, 67–76. [https://doi.org/10.1016/0022-0248\(86\)90249-6](https://doi.org/10.1016/0022-0248(86)90249-6)
- Ravi Sankar, H., Parameswaran, V., 2016. Effect of multiple holes on dynamic buckling of stubby shells: An experimental and numerical investigation. *Int. J. Impact Eng.* 96, 129–145. <https://doi.org/10.1016/j.ijimpeng.2016.05.014>
- Samantaray, D., Mandal, S., Bhaduri, A.K., 2009a. A comparative study on Johnson Cook,

- modified Zerilli-Armstrong and Arrhenius-type constitutive models to predict elevated temperature flow behaviour in modified 9Cr-1Mo steel. *Comput. Mater. Sci.* 47, 568–576. <https://doi.org/10.1016/j.commatsci.2009.09.025>
- Samantaray, D., Mandal, S., Bhaduri, A.K., Venugopal, S., Sivaprasad, P. V, 2011. Analysis and mathematical modelling of elevated temperature flow behaviour of austenitic stainless steels. *Mater. Sci. Eng. A* 528, 1937–1943. <https://doi.org/https://doi.org/10.1016/j.msea.2010.11.011>
- Samantaray, D., Mandal, S., Borah, U., Bhaduri, A.K., Sivaprasad, P. V, 2009b. A thermo-viscoplastic constitutive model to predict elevated-temperature flow behaviour in a titanium-modified austenitic stainless steel. *Mater. Sci. Eng. A* 526, 1–6. <https://doi.org/https://doi.org/10.1016/j.msea.2009.08.009>
- Senkov, O.N., Wilks, G.B., Miracle, D.B., Chuang, C.P., Liaw, P.K., 2010. Refractory high-entropy alloys. *Intermetallics* 18, 1758–1765. <https://doi.org/10.1016/J.INTERMET.2010.05.014>
- Shi, Y., Yang, B., Liaw, P., 2017. Corrosion-Resistant High-Entropy Alloys: A Review. *Metals (Basel)*. 7, 43. <https://doi.org/10.3390/met7020043>
- Siddique, S., Imran, M., Walther, F., 2017. Very high cycle fatigue and fatigue crack propagation behavior of selective laser melted AlSi12 alloy. *Int. J. Fatigue* 94, 246–254. <https://doi.org/10.1016/j.ijfatigue.2016.06.003>
- Sinha, S., Nene, S.S., Frank, M., Liu, K., Agrawal, P., Mishra, R.S., 2019. On the evolving nature of c/a ratio in a hexagonal close-packed epsilon martensite phase in transformative high entropy alloys. *Sci. Rep.* 9, 1–14. <https://doi.org/10.1038/s41598-019-49904-5>
- Sinha, S., Nene, S.S., Frank, M., Liu, K., Lebensohn, R.A., Mishra, R.S., 2020. Deformation mechanisms and ductile fracture characteristics of a friction stir processed transformative high entropy alloy. *Acta Mater.* 184, 164–178. <https://doi.org/10.1016/j.actamat.2019.11.056>
- Soares, G.C., Patnamsetty, M., Peura, P., Hokka, M., 2019. Effects of Adiabatic Heating and Strain Rate on the Dynamic Response of a CoCrFeMnNi High-Entropy Alloy. *J. Dyn. Behav. Mater.* 5, 320–330. <https://doi.org/10.1007/s40870-019-00215-w>
- Song, B., Sanborn, B., 2019. A Modified Johnson–Cook Model for Dynamic Response of Metals with an Explicit Strain- and Strain-Rate-Dependent Adiabatic Thermosoftening Effect. *J. Dyn. Behav. Mater.* 5, 212–220. <https://doi.org/10.1007/s40870-019-00203-0>
- Sonkusare, R., Jain, R., Biswas, K., Parameswaran, V., Gurao, N.P., 2020. High strain rate compression behaviour of single phase CoCuFeMnNi high entropy alloy. *J. Alloys Compd.* 823, 153763. <https://doi.org/10.1016/j.jallcom.2020.153763>
- Stanford, N., Dunne, D.P., 2010. Effect of Si on the reversibility of stress-induced martensite in Fe–Mn–Si shape memory alloys. *Acta Mater.* 58, 6752–6762. <https://doi.org/10.1016/J.ACTAMAT.2010.08.041>
- Tan, J.Q., Zhan, M., Liu, S., Huang, T., Guo, J., Yang, H., 2015. A modified Johnson–Cook model for tensile flow behaviors of 7050-T7451 aluminum alloy at high strain rates. *Mater.*

Sci. Eng. A 631, 214–219. <https://doi.org/https://doi.org/10.1016/j.msea.2015.02.010>

Thapliyal, S., Komarasamy, M., Shukla, S., Zhou, L., Hyer, H., Park, S., Sohn, Y., Mishra, R.S., 2019. An integrated computational materials engineering-anchored closed-loop method for design of aluminum alloys for additive manufacturing. Materialia 100574. <https://doi.org/10.1016/J.MTLA.2019.100574>

Thapliyal, S., Nene, S.S., Agrawal, P., Wang, T., Morphew, C., Mishra, R.S., McWilliams, B.A., Cho, K.C., 2020. Damage-tolerant, corrosion-resistant high entropy alloy with high strength and ductility by laser powder bed fusion additive manufacturing. Addit. Manuf. 36, 101455. <https://doi.org/10.1016/j.addma.2020.101455>

Wang, B., Fu, A., Huang, X., Liu, B., Liu, Y., Li, Z., Zan, X., 2016. Mechanical Properties and Microstructure of the CoCrFeMnNi High Entropy Alloy Under High Strain Rate Compression. J. Mater. Eng. Perform. 25, 2985–2992. <https://doi.org/10.1007/s11665-016-2105-5>

Wang, B., Liu, Z., Song, Q., Wan, Y., Ren, X., 2019. A Modified Johnson–Cook Constitutive Model and Its Application to High Speed Machining of 7050-T7451 Aluminum Alloy. J. Manuf. Sci. Eng. 141. <https://doi.org/10.1115/1.4041915>

Wang, X., Huang, C., Zou, B., Liu, H., Zhu, H., Wang, J., 2013. Dynamic behavior and a modified Johnson–Cook constitutive model of Inconel 718 at high strain rate and elevated temperature. Mater. Sci. Eng. A 580, 385–390. <https://doi.org/https://doi.org/10.1016/j.msea.2013.05.062>

Wei, H.L., Mazumder, J., DebRoy, T., 2015. Evolution of solidification texture during additive manufacturing. Sci. Rep. 5, 16446. <https://doi.org/10.1038/srep16446>

Wei, S., Kim, J., Tasan, C.C., 2019. Boundary micro-cracking in metastable Fe45Mn35Co10Cr10 high-entropy alloys. Acta Mater. 168, 76–86. <https://doi.org/10.1016/J.ACTAMAT.2019.01.036>

Yadav, S., Sarkar, S., Aggarwal, A., Kumar, A., Biswas, K., 2018. Wear and mechanical properties of novel (CuCrFeTiZn)100-xPbx high entropy alloy composite via mechanical alloying and spark plasma sintering. Wear 410–411, 93–109. <https://doi.org/10.1016/j.wear.2018.05.023>

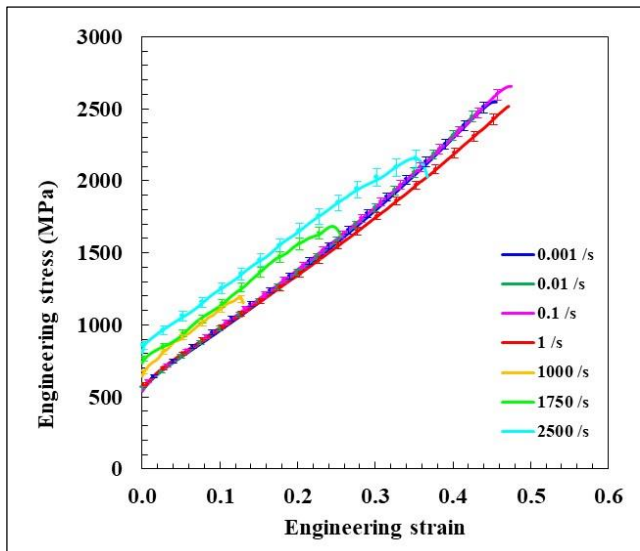
Yang, Z., Yang, M., Ma, Y., Zhou, L., Cheng, W., Yuan, F., Wu, X., 2020. Strain rate dependent shear localization and deformation mechanisms in the CrMnFeCoNi high-entropy alloy with various microstructures. Mater. Sci. Eng. A 793, 139854. <https://doi.org/10.1016/j.msea.2020.139854>

Yi, S.-B., Davies, C.H.J., Brokmeier, H.-G., Bolmaro, R.E., Kainer, K.U., Homeyer, J., 2006. Deformation and texture evolution in AZ31 magnesium alloy during uniaxial loading. Acta Mater. 54, 549–562. <https://doi.org/10.1016/J.ACTAMAT.2005.09.024>

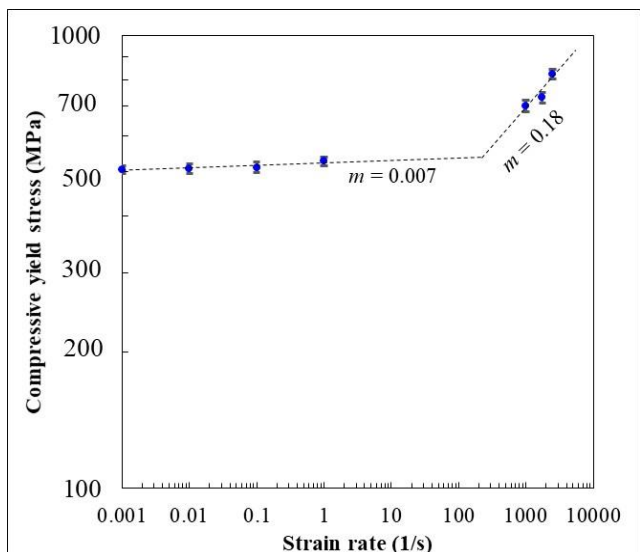
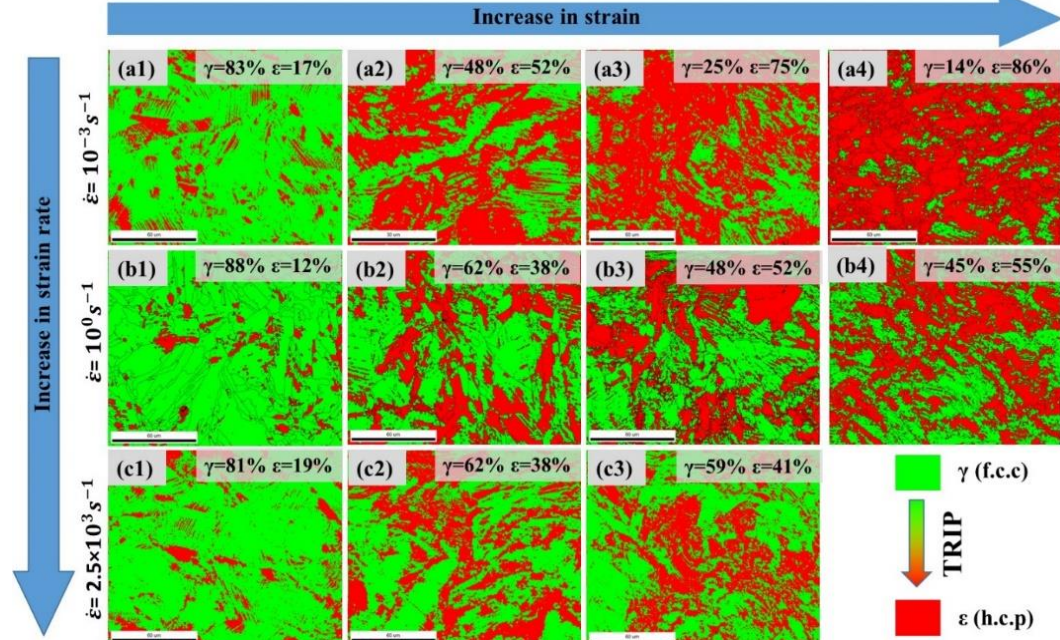
Yin, F., Hu, S., Xu, R., Han, X., Qian, D., Wei, W., Hua, L., Zhao, K., 2020. Strain rate sensitivity of the ultrastrong gradient nanocrystalline 316L stainless steel and its rate-dependent modeling at nanoscale. Int. J. Plast. 129, 1–18. <https://doi.org/10.1016/j.ijplas.2020.102696>

- Zerilli, F.J., 2004. Dislocation mechanics-based constitutive equations. *Metall. Mater. Trans. A Phys. Metall. Mater. Sci.* 35 A, 2547–2555. <https://doi.org/10.1007/s11661-004-0201-x>
- Zerilli, F.J., Armstrong, R.W., 1997. Dislocation mechanics based analysis of material dynamics behavior: Enhanced ductility, deformation twinning, shock deformation, shear instability, dynamic recovery. *J. Phys. IV* 7, 637–642. <https://doi.org/10.1051/jp4:19973109>
- Zerilli, F.J., Armstrong, R.W., 1992. The effect of dislocation drag on the stress-strain behavior of F.C.C. metals. *Acta Metall. Mater.* 40, 1803–1808. [https://doi.org/10.1016/0956-7151\(92\)90166-C](https://doi.org/10.1016/0956-7151(92)90166-C)
- Zhang, D.-N., Shangguan, Q.-Q., Xie, C.-J., Liu, F., 2015. A modified Johnson–Cook model of dynamic tensile behaviors for 7075-T6 aluminum alloy. *J. Alloys Compd.* 619, 186–194. <https://doi.org/https://doi.org/10.1016/j.jallcom.2014.09.002>
- Zhang, F., Liu, Z., Wang, Y., Mao, P., Kuang, X., Zhang, Z., Ju, Y., Xu, X., 2020. The modified temperature term on Johnson-Cook constitutive model of AZ31 magnesium alloy with {0002} texture. *J. Magnes. Alloy.* 8, 172–183. <https://doi.org/https://doi.org/10.1016/j.jma.2019.05.013>
- Zhang, T.W., Ma, S.G., Zhao, D., Wu, Y.C., Zhang, Y., Wang, Z.H., Qiao, J.W., 2020. Simultaneous enhancement of strength and ductility in a NiCoCrFe high-entropy alloy upon dynamic tension: Micromechanism and constitutive modeling. *Int. J. Plast.* 124, 226–246. <https://doi.org/10.1016/j.ijplas.2019.08.013>
- Zhao, L., Guo, Q., Li, Z., Li, Z., Fan, G., Xiong, D.B., Su, Y., Zhang, J., Tan, Z., Zhang, D., 2018. Strain-rate dependent deformation mechanism of graphene-Al nanolaminated composites studied using micro-pillar compression. *Int. J. Plast.* 105, 128–140. <https://doi.org/10.1016/j.ijplas.2018.02.006>
- Zhou, R., Liu, Y., Zhou, C., Li, S., Wu, W., Song, M., Liu, B., Liang, X., Liaw, P.K., 2018. Microstructures and mechanical properties of C-containing FeCoCrNi high-entropy alloy fabricated by selective laser melting. *Intermetallics* 94, 165–171. <https://doi.org/10.1016/j.intermet.2018.01.002>
- Zhu, Z.G., Nguyen, Q.B., Ng, F.L., An, X.H., Liao, X.Z., Liaw, P.K., Nai, S.M.L., Wei, J., 2018. Hierarchical microstructure and strengthening mechanisms of a CoCrFeNiMn high entropy alloy additively manufactured by selective laser melting. *Scr. Mater.* 154, 20–24. <https://doi.org/10.1016/j.scriptamat.2018.05.015>

Mechanical response



Phase evolution



Texture evolution

